STUDY OF CERIA NANOPARTICLES SYNTHESIS AND THE PERFORMANCE OF NANO-CERIA COATING FOR HIGH TEMPERATURE OXIDATION RESISTANCE IN COMBUSTION ATMOSPHERE

by

Lingke Mao

A Thesis Submitted in
Partial Fulfillment of the
Requirement for the Degree of

Master of Science
in Engineering

at

The University of Wisconsin-Milwaukee
May 2016

ABSTRACT

STUDY OF CERIA NANOPARTICLES SYNTHESIS AND THE PERFORMANCE OF NANO-CERIA COATING FOR HIGH TEMPERATURE OXIDATION RESISTANCE IN COMBUSTION ATMOSPHERE

by
Lingke Mao

The University of Wisconsin-Milwaukee, 2016
Under the Supervision of Dr. Benjamin Church

Ceria (CeO_2) nanoparticles were synthesized by the microemulsion method with Bis(2-ethylhexyl) Sulfosuccinate Sodium Salt (AOT) as the surfactant. Stirring speed during synthesis was used to optimize the process and a precipitation process was applied to dilute the surfactant. The prepared ceria nanoparticles were characterized by x-ray diffraction (XRD) and transmission electron microscopy (TEM). As the result, non-agglomerated and time-stable ceria nanoparticles were obtained with the average particles size of 2-3 nanometers. Stainless steel 316L substrates were coated by a dipping method with the help of a slide motor which provided constant speed and uniform coating layers. Both coated and uncoated SS316L samples were oxidized in dry air and combustion atmospheres to determine the effect of the nanoparticles on oxidation performance. The oxidation temperature of dry air was 800°C -900°C and that of combustion atmosphere was 650°C -850°C. The kinetic mass gaining was recorded by a thermo-gravimetric analysis system and the samples after tests were characterized by scanning electron microscopy (SEM) and XRD.

According to the TGA data, the effectiveness of ceria coating was verified in the dry air. However in the combustion atmosphere, the oxidation was complicated and the whole process could be divided into three parts: an initial slow oxidation stage, an accelerating stage and a third parabolic stage. The possible reason could be the initial protection and subsequent volatilization of Cr_2O_3. A hypothesis of the mechanism was proposed in this study to explain the formation of these three stages. The effect of ceria nanoparticles in combustion atmosphere was highly dependent on temperature with a benefit observed only at low temperature. Mechanisms responsible for the influence of ceria on oxidation in combustion atmosphere remained unclear.

TABLE OF CONTENTS

LIST OF FIGURES

LIST OF TABLES

LIST OF ABBREVIATIONS

Thermogravimetric Analysis ---------- TGA

Stainless Steel 316L ---------- SS316L

Bis(2-ethylhexyl) Sulfosuccinate Sodium Salt ---------- AOT

X-ray diffraction ----------- XRD

Transmission Electron Microscope ---------- TEM

Scanner Electron Microscope ---------- SEM

Revolutions Per Minute ----------RPM

Full Width for the Half Maximum Intensity for the Peak ----------- FMHM

ACKNOWLEDGEMENTS

I would like to thank my advisor Professor Benjamin Church for his invaluable guidance, positive influence and the equipment supporting to make all this study possible.

To thank Dr. Steve Hardcastle from the Advanced Analytical Facilities (AAF) for his assistance on XRD characterization.

To thank my committee, Dr. Hugo Lopez and Dr. Benjamin Schultz.

To thank my group members, Shengyi Li, Yangping Sheng, Bryce Erwin for their help during the study.

To thank Dr. Junjie Niu and Yan Zhang and Chao Cheng for their assistance on TEM characterization.

To thank my mother and father for their financial support and encouragement.

1 Introduction

Cerium oxide as a coating material has shown significant benefit for protection of high temperature oxidation [1-3]. On this basis, various studies of cerium oxide have been performed to study the property of this coating in different synthetic methods and oxidation situations. Patil and Seal's group studied the synthesis of nano-crystalline ceria by microemulsion method [4] and the effect of trivalent rare earth dopants [5]. Murray's group studied the ceria used in the anode of high temperature full cell which improved the power density at operation temperature[6] and Rotavera 's group studied the Effect of ceria nanoparticles on soot inception which found ceria can delay the growing of soot [7]. As well as the oxidation tests, the mechanisms also have been put forwarded by various researchers. Peakall's group suggest that ceria remit the stress between substrate and oxide scale causing by different thermal expansion coefficients [8]. Stringer's group suggest that the "reactive element effect" (REE) of ceria accelerates the formation of chromium oxide on the surface of stainless steel [9]. Some other groups believe the improvement of oxidation resistance should contribute to the diffusion mechanism: ceria coating reverses the diffusion speed for both iron and oxygen [10-11].

However, high temperature oxidation in the presence of water vapor can result in volatilization of Cr_2O_3 which could cause serious oxidation and overturn the theoretical basis of protection mechanism for Cr_2O_3 in dry air [12-14]. Besides, water vapor enhances the oxygen transport in the oxide layer and the internal oxidation rate[15-16]. Under a different atmosphere and switched mechanism, the performance of cerium oxide coating is still unclear. The coating method of high temperature oxidation protection is under suspicion.

This study focuses on the ceria coating performance in combustion atmosphere, which is a possible atmosphere for high temperature fuel cells, power generation equipments or turbines. By directly burning CH_4, both water vapor and carbon dioxide are involved at their initial presence. Coated and uncoated samples are tested for comparison. A Thermogravimetric Analysis (TGA) system is used to record the kinetic data. By using TGA system, more details of oxidation mechanism can be revealed.

The improvement of cerium oxide synthesis and coating process is also a part of this study. The goal is to obtain non-agglomerated ceria nanoparticles, that are stabile for long time periods, and easily applied to a coating process. Based on microemulsion method, repetitive precipitation is used to purify the ceria from the surfactant rather removing the surfactant through heating and decompose it which would also induce unwanted particle growth. A slide motor is used in dip coating as well to reduce the agglomeration during coating

2 Background

2.1 Thermodynamics of high temperature oxidation

For all the chemical reactions, the second law of thermodynamics can predict whether it can happen or not. One of the most conveniently written of second law is the equation of Gibbs free energy, equation 1.

$$G' = H' - TS' \qquad \text{eq.1}$$

Where G' is the Gibbs free energy, H' is the enthalpy and S' is the entropy of the system. A general oxidation reaction can be written in equation 2.

$$x\frac{b}{a}\mathrm{Me}(s) + O_2(g) = \frac{b}{a}\ \mathrm{Me}_xO_{\frac{2a}{b}}(s) \qquad \text{eq.2}$$

Where Me is metal and the change of Gibbs free energy can be expressed as in equation 3.

$$\Delta G' = \Delta G^o + RT\frac{a(\mathrm{Me}_xO_{2a/b})^{b/a}}{a(\mathrm{Me})^{xb/a}a(O_2)} \qquad \text{eq.3}$$

Where ΔG is the Gibbs free energy change when all species at their standard states and a is the thermodynamic activity. When the reaction reaches balance, $\Delta G'$=0. If the thermodynamic activities of medal and medal oxide are constant. Then the equation 3 can be written as equation 4:

$$\Delta G^o = -RT\frac{1}{a(O)_2} \qquad \text{eq.4}$$

In dry air, $a(O)_2$ =pO_2. Then the equation 4 is written in equation 5:

$$\Delta G^o = -RT\frac{1}{pO_2} \qquad \text{eq.5}$$

or equation 6:

$$\Delta G^o = RT\ \ pO_2 \qquad \text{eq.6}$$

Thus the ΔG^{o} can be plotted as the variation of temperature. The Ellingham diagram of ΔG^{o} and temperature is shown in Figure 1, Standard free energy of formation of selected oxides as a function of temperature. According to the Ellingham, the decomposition pressure of each oxides can be predicted at given temperature[17].

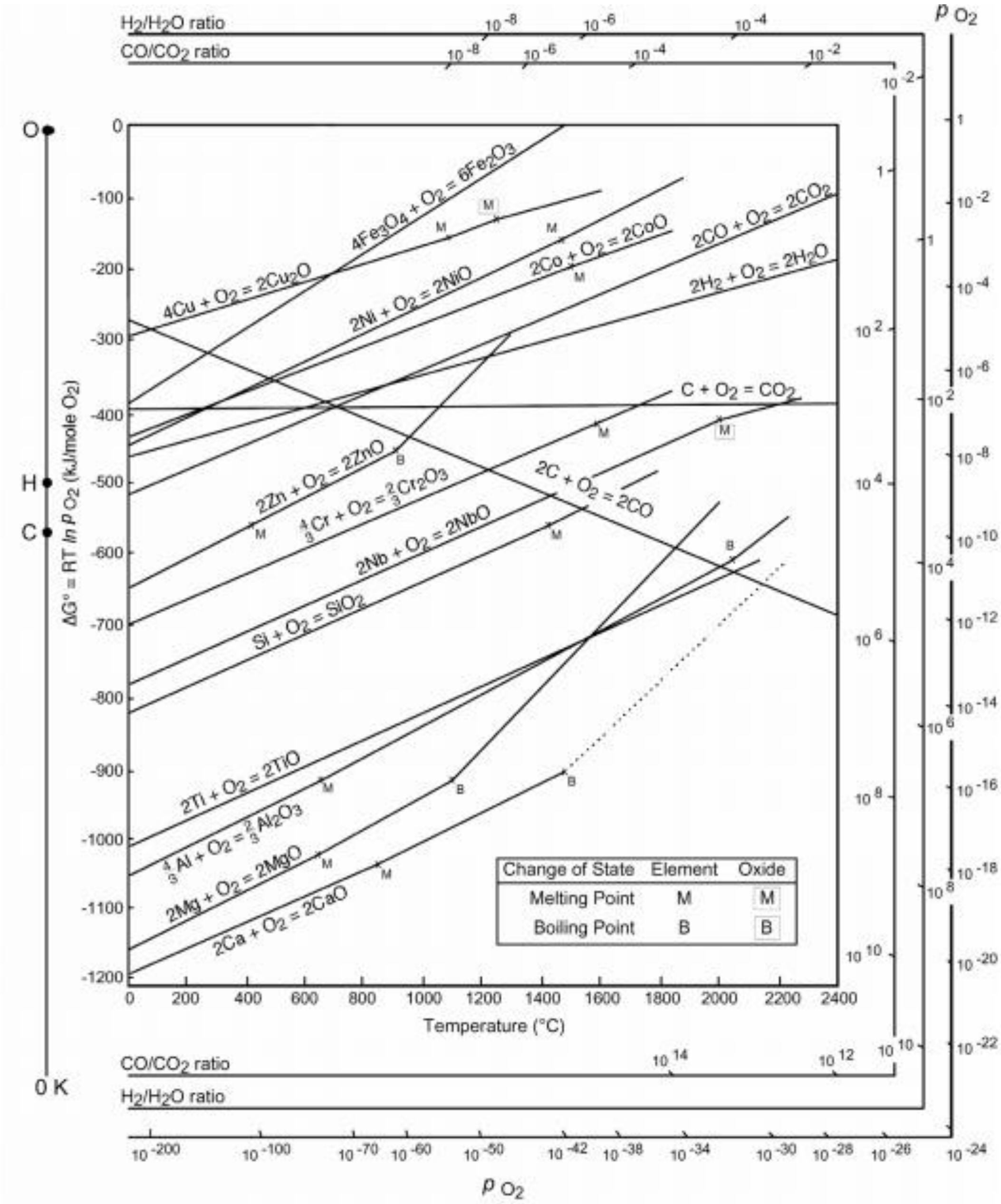

Figure 1, Standard free energy of formation of selected oxides as a function of temperature.[17]

2.2 Mechanisms of high temperature oxidation

2.2.1 Diffusion controlled oxidation

If the metal ion transport across the growing oxide layer controls the rate of oxidation and the thermodynamic equilibrium is established at each interface, the process can be expressed as in equation 7 [17]:

$$j_{M^{a+}} = -j_{V_M} = D_{V_M}\frac{C''_{V_M}-C'_{V_M}}{x} \qquad \text{eq.7}$$

Where *x* is the oxide thickness, $j_{M^{a+}}$ is the outward metal ion flux, D_{V_M} is the diffusion coefficient for metal vacancies, and C''_{V_M} and C'_{V_M} are the vacancy concentration at the scale-metal and scale-gas interfaces, respectively. Once the equilibrium reaches, in equation 8:

$$k = D_{V_M}\left(C''_{V_M} - C'_{V_M}\right)k' \qquad \text{eq.8}$$

k is a constant and we have equation 9:

$$j_{M^{a+}} = \frac{dx}{dt} = \frac{k}{x} \qquad \text{eq.9}$$

The integration of equation 9 with *x* and *t* can't be 0 is in equation 10:

$$x^2 = 2kt \qquad \text{eq.10}$$

which is the common parabolic rate law. Furthermore, the C_{VM} can be replaced by oxygen partial pressure in equation 11:

$$C_{V_M} = \text{const}\ p_{O_2}^{1/n} \qquad \text{eq.11}$$

Thus, in equation 12:

$$k = \text{const}[\left(p''_{O_2}\right)^{1/n} - \left(p'_{O_2}\right)^{1/n}] \qquad \text{eq.12}$$

and we neglect the small quantity $\left(p'_{O_2}\right)^{1/n}$, the equation can be expressed in equation 13:

$$x^2 = 2k''\left(p''_{O_2}\right)^{1/n}t \qquad \text{eq.13}$$

2.2.2 Wagner theory of oxidation

Wagner theory is based on the assumptions listed below [17-18]

- The oxide layer is a compact, perfectly adherent scale.
- Migrations of ions or electrons across the scale is the rate-controlling process.
- Thermodynamic equilibrium is established at both the metal-scale and scale-gas interfaces.
- The oxide scale shows only small deviations from stoichiometry and, hence, the ionic fluxes are independent of position within the scale.
- Thermodynamic equilibrium is established locally throughout the scale.
- The scale is thick compared with the distance over which space charge effects occur.
- Oxygen solubility in the metal may be neglected.

Figure 2 shows the diagram of scale formation according to Wagner's model. Both metal ions and oxygen ions have tendency to cross the oxide scale. This migration will cause an electric field and at last a balanced and no net charge transfer is obtained. Being charged particles, ions will under the influence of both chemical and electrical potential gradients, and the whole driving force can be expressed as equation 14:

$$\mathrm{j_i = C_i v_i = -\frac{C_i B_i}{N_A}\left(\frac{\partial \mu_i}{\partial x} + Z_i F \frac{\partial \emptyset}{\partial x}\right)} \qquad \text{eq.14}$$

where *j_i* is the flux of particles, *C_i* is the concentration of ion *i*, *v_i* is the proportional to the acting force and *B_i* is the particle mobility. *N_A* and *F* are Avogadro's constant and Faraday constant, respectively.

Besides, the balance of electrical neutrality is given by equation 15:

$$\mathrm{Z_c j_c + Z_e j_e = 0} \qquad \text{eq.15}$$

where Z_c and Z_e are the charge on cations and electrons respectively. The balance of ionization of metal is given by equation 16:

$$\mu_M = \mu_c + Z_c\mu_e \qquad \text{eq.16}$$

so the combination of equation 14-16 finally reach the conclusive equation 17:

$$k = \frac{1}{RT}\int_{\mu_M''}^{\mu_M'} D_M \, d_{\mu_M}$$

$$k = \frac{1}{RT}\int_{\mu_X''}^{\mu_X'} D_X \, d_{\mu_X} \qquad \text{eq.17}$$

where k is partial electrical conductivity of anions D_M and D_X are the diffusion coefficient for metal and oxygen, respectively. According to equation 17, a parabolic relationship between D_i and μ_i can be obtained. As well as that in diffusion controlled oxidation, the high temperature oxidation in dry air can be regarded as a parabolic form process [19-20].

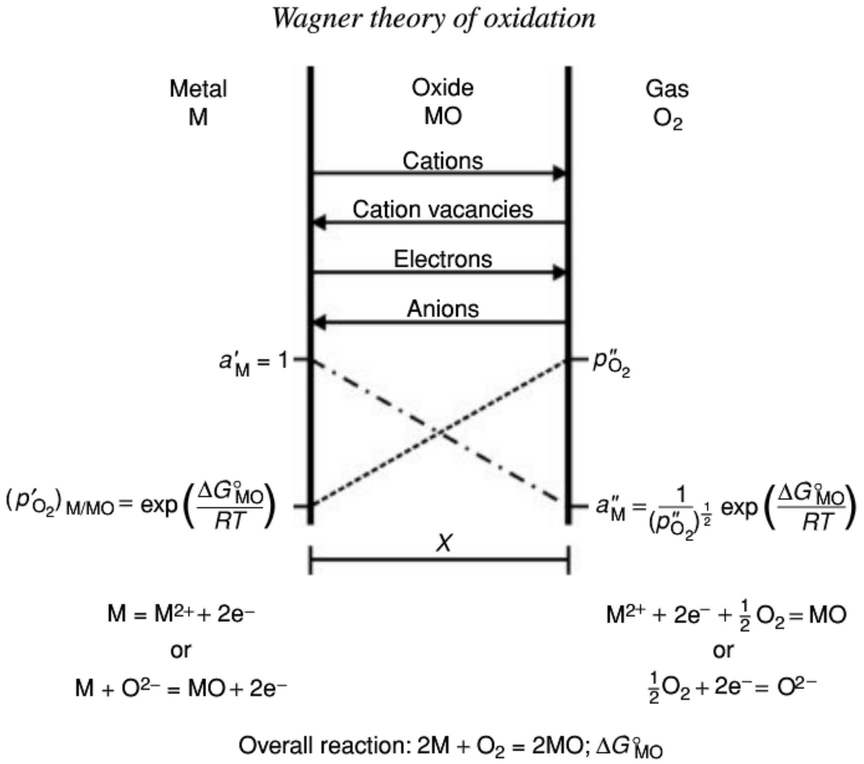

Figure 2, diagram of scale formation according to Wagner's model.[18]

2.3 Protective Cr_2O_3 and its volatilization

In dry air atmosphere, Cr in the stainless steel can form a dense Cr_2O_3 protective layer. This Cr_2O_3 is usually considered to be the main reason of the outstanding high temperature oxidation resistance of stainless steel [21-22]. Cr_2O_3 acts as a physical barrier protect the further oxidation of iron-rich substrate. At higher temperature, Cr_2O_3 transforms to spinel oxide $FeCr_2O_4$. During oxidation, $FeCr_2O_4$ becomes progressively richer in iron up to the transformation in hematite. The growth of oxide layer obey the Wagner model and parabolic law [23-24].

Some oxides including Cr_2O_3 volatilize at high temperature when water vapor is presence. The general reaction of volatilization is shown in equation 18:

$$\frac{1}{p}\mathrm{M_pO_q} + \mathrm{mH_2O} + \mathrm{nO_2} = \mathrm{MO_{\frac{q}{p}+m+2n}H_{2m}}\ (\mathrm{g}) \qquad \text{eq.18}$$

and the reaction for Cr_2O_3 is equation 19:

$$\mathrm{2Cr_2O_3 + 4H_2O + 3O_2 = 4CrO_2(OH)_2}\ (\mathrm{g}) \qquad \text{eq.19}$$

The $\Delta H^0_{r,298}$ of reaction is 55.34 kJ/mol and the $\Delta S^0_{r,298}$ is -41.51J/mol K. The partial pressure of $\mathrm{CrO_2(OH)_2}$ is $1.97\text{x}10^{-6}$ at 873K when $p_{H2O}=1$ and $p_{O2}=0.5$.

Another possible reaction of Cr_2O_3 volatilization is shown in equation 20:

$$\mathrm{2Cr_2O_3 + 3O_2 = 4CrO_3}\ (\mathrm{g}) \qquad \text{eq.20}$$

The Cr_2O_3 volatilization becomes dominating only when the temperature higher than 1200 °C. The formation of $\mathrm{CrO_3}$ in dry air can be neglected at 800-900 ^{o}C when comparing with $\mathrm{CrO_2(OH)_2}$ formation in water vapor atmosphere [12].

2.4 Austenitic Stainless Steel 316L

Stainless steel contains chromium which provides the unique stainless and corrosion resisting properties. There are five major types of stainless steel.

- Austenitic stainless steels are 200 series or 300 series. They are non magnetic and have high corrosion resistance. They can be hardened only by cold working - not by heat treatment. They are highly formable. But, they are prone to stress corrosion cracking.
- Ferrite stainless steels are 400 series. They are magnetic. They have lower ductility and lower corrosion resistance than the austenitic grades. But, they offer high resistance to stress corrosion cracking. They are hardened by cold working and are not heat treatable.
- Martensitic stainless steels are 400 series and 500 series. They are magnetic. They have higher strength, higher wear resistance and higher fatigue resistance than the austenitic and ferrite grades. They can also be heat treated. But, corrosion resistance is moderate and lower than the austenitic and ferrite grades.
- Precipitation Hardening Grade Stainless Steels are also called PH types. Their corrosion resistance is equivalent to that of austenitic grades and strength is generally higher than that of martensitic grades. They also retain high strength at elevated temperatures.
- Duplex stainless steels are mixture of austenitic and ferrite. They provide higher corrosion resistance than the austenitic stainless steels. They are also more resistant to stress corrosion cracking than the austenitic stainless steels. They have higher strength than the austenitic grades.

Alloy austenitic stainless steel 316/316L is a chromium-nickel molybdenum stainless steel developed to provide improved corrosion resistance to Alloy 304/304L in moderately corrosive environments. It also provides higher creep, stress-to-rupture and tensile strength at elevated temperatures.

SS 316L has good oxidation resistance performance up to the temperature of 900°C even though it is not recommended for a continuous use above 425°C. SS 316L are non-hardenable by heat treatment but the common cold working operations can be applied on the SS 316L. Post work annealing should be carried out to remove internal stresses. Machining and forming SS 316L is recommended to be down at low speed and constant feed rate to avoiding work hardening.

2.5 Cerium oxide

Cerium(IV) oxide is an oxide of rare earth metal cerium, the chemical formula of cerium(IV) oxide is Ce_2O. Cerium is the most abundant of the rare earth elements and is found in a number of minerals including allanite, monazite, bastnasite and synchysite. The production of cerium involves separation from other rare earth metals and chemical treatment. Pure cerium can be obtained by reduction of cerium (III) chloride.

As a typically rare earth metal, the energies of 4f, 5d and 6s orbital are very close. Therefore cerium has 3 possible oxidation states +2, +3 and +4. The oxidation state of +2 is rare as the materials including CeH_2 ,CeS and CeI_2 . Ce(III) and Ce(IV) are common and the most stable compound is CeO_2 [25].

In this research, CeO_2 is been chosen as the coating material for high temperature oxidation. Figure 3 shows the FFC structure for CeO_2 crystal [26].

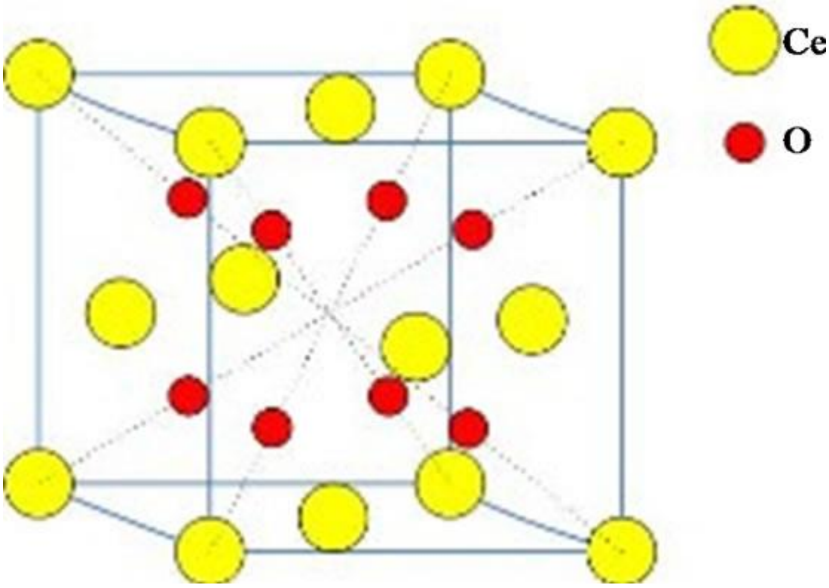

Figure 3, FCC structure for CeO_2 .

The CeO_2 is synthesized from $Ce(NO_3)_3$ to obtain nano scale particles. The Ce^{3+} ions in solution are oxidized by NH_4OH and form $Ce(OH)_4$ solid. Then the $Ce(OH)_4$ dehydrate to form CeO_2 . The whole chemical reaction of this process is too complicate to write down due to the involving of surfactant and the incompletion of the reaction [6-7].

The prefect CeO_2 crystal has a FCC structure with the oxygen atom has four coordinated and cerium atom has eight coordinated. Usually, CeO_2 prepared for coating presences as a non-stoichiometric oxide that is a mixture of Ce(III) oxide and Ce(IV) oxide, while still retaining the FCC structure [27].

A hypothesis was supposed to explain the improvement high temperature oxidation protection by using nano CeO_2. The oxidation rate is controlled by the outward diffusion of chromium layer. This hypothesis assumes that large Ce^{4+} ions form pairs with metal vacancies in oxide grain boundaries. These dense array of pairs block the metal cation diffusion while allowing oxygen ion diffusion to continue. As a result, the switch of dominant oxidation mechanism from outward metal diffusion to inward oxygen diffusion and the oxidation rate reduced by 1-2 orders of magnitude [28].

2.6 Coating

Coating technology has been widely used in the engineering as important part of surface treatment. The purpose of functional coating can be light reflecting improvement, physical protecting, anti-corrosion or changing adhesion properties. Hundreds of coating methods are been using for various coating propose. In this part, only high temperature coating is discussed because this coating has more strict requirements and more difficulties in engineering.[29-31]

For high temperature coating, five significant engineering factors must be considered:

- Metallurgical compatibility. The interdiffusion and chemical reaction between coating materials and substrates must be at a acceptable degree. The excessive reaction can result in the degradation of both aspects and reduce the lifetime of materials.
- Coating process compatibility. As well as in the metallurgical compatibility, the compatibility during the process also must be controlled. This would happen in the process of high temperature or special coating treatments.
- Mechanical compatibility. For high temperature, the coefficient of thermal expansion can be the most important factor. Besides, the internal from thermal cycle is also a challenge for the coating adhesion.
- Component coatability. This is technology issue that the coating process must match the geometry and size of the component. Sometime the processes must be done inside an enclosed tank or reactor.

- Atmosphere compatibility. The atmosphere for high temperature use is much harsher than room temperature. Sometime corrosive or active components can be present in the atmosphere. The coating material should have compatibility for all possible atmospheres.

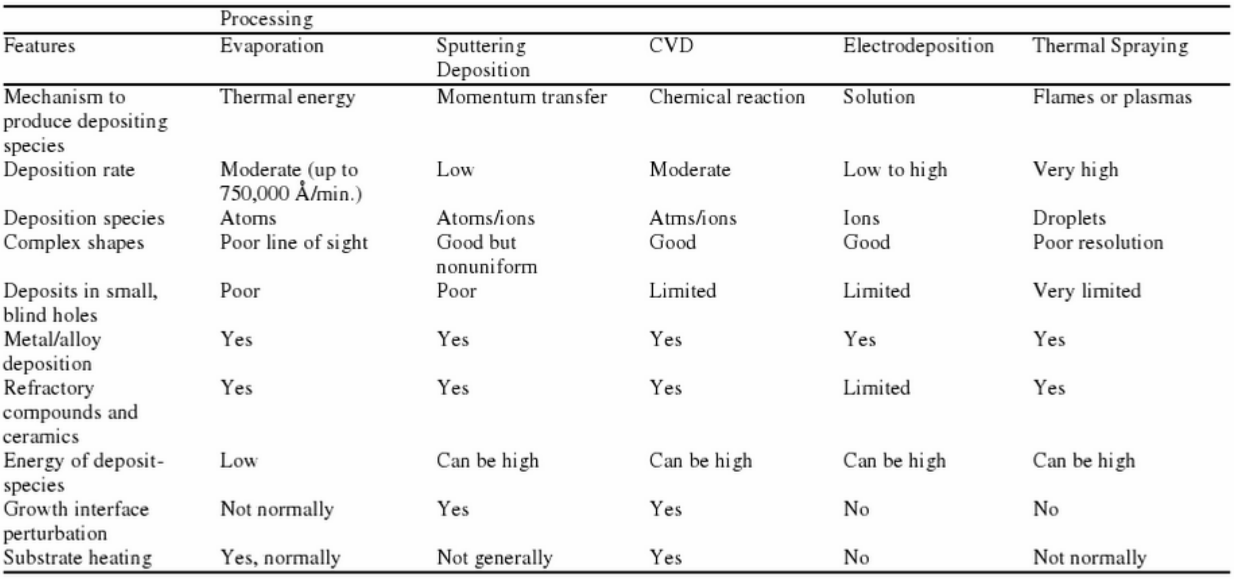

	Processing				
Features	Evaporation	Sputtering Deposition	CVD	Electrodeposition	Thermal Spraying
Mechanism to produce depositing species	Thermal energy	Momentum transfer	Chemical reaction	Solution	Flames or plasmas
Deposition rate	Moderate (up to 750,000 Å/min.)	Low	Moderate	Low to high	Very high
Deposition species	Atoms	Atoms/ions	Atms/ions	Ions	Droplets
Complex shapes	Poor line of sight	Good but nonuniform	Good	Good	Poor resolution
Deposits in small, blind holes	Poor	Poor	Limited	Limited	Very limited
Metal/alloy deposition	Yes	Yes	Yes	Yes	Yes
Refractory compounds and ceramics	Yes	Yes	Yes	Limited	Yes
Energy of deposit-species	Low	Can be high	Can be high	Can be high	Can be high
Growth interface perturbation	Not normally	Yes	Yes	No	No
Substrate heating	Yes, normally	Not generally	Yes	No	Not normally

Figure 4, the benefits and limitations of different kinds of coating methods.[30]

In this part, several kinds of important coating methods will be discussed and the benefits/limitations of each coating methods are summarized in figure 4. Evaporation process is an atomistic deposition method that involves the vaporizations and deposition. The advantage of evaporation is its wide range of materials and substrate shapes, while the limitations are only complete coating can be applied by this method. Sputtering deposition is another physical deposition without evaporation. The advantage of sputtering is also its wide range of coating materials and the limitation is the lack of interdiffusion during deposition. The benefits of chemical vapor deposition process is the coating can be fixed at the part of substrate however it requires the chemical reaction or strong interdiffusion between coating materials and substrate. Thermal spraying has a high deposition rate and has a thick coating layer at meanwhile.

3 Experimental procedures

3.1 Synthesis of ceria nanoparticles.

Ceria nanoparticles were synthesized by microemulsion method with the Bis(2-ethylhexyl) Sulfosuccinate Sodium Salt (AOT) as the surfactant. Ce^{3+} ions were oxidized to Ce^{4+} by NH_4OH and then formed $Ce(OH)_4$. At last $Ce(OH)_4$ dehydrated and CeO_2 was obtained.

The main chemicals used in the experiment were: cerium(III) nitrate hexahydrate (Ce(NO3)·6H2O), 99%, purchased from Aldrich Chemicals Company, Inc. Toluene, 99.9%, purchased from Aldrich Chemicals Company, Inc. Ammonium hydroxide, 30% w/w, purchased from Aldrich Chemicals Company, Inc. Bis(2-ethylhexyl) Sulfosuccinate Sodium Salt (AOT), 95%, purchased from Tokyo Chemical Industry co., LTD.

Using the characteristics of precipitation in the synthesis process, surfactant AOT was diluted by removing upper toluene layer and the CeO_2 was purified successfully. Some important synthesis procedure factors such as temperature, stirring speed, stirring time and the amount of chemistry reagent were also tested to find a preferable agglomeration degree and particle size. The prepared ceria nanoparticles were stored in toluene solution for further use. Additional details of procedure specific to the processing variables used are embedded in the results section.

3.2 Preparation of SS 316L substrate.

Stainless steel 316L was chosen to be the oxidation material for its wide use and good high temperature performance. Table 1 shows the composition ranges for SS 316L.

composition	Fe	C	Mn	Si	P	S	Cr	Mo	Ni	N
Min	Bal	-	-	-	-	-	16	2	10	-
Max	Bal	0.03	2	0.75	0.045	0.03	18	3	14	0.10

Table 1, Composition ranges for 316L stainless steel (%).

The purchased SS 316L thin plate was cut into small size pieces of 20mm x 10mm. Then the SS 316 small substrates were grinded and polished with SiC sand paper until 1000 grit. One or two small holes were punched on the polished substrates. There holes were used for hanging during the coating or oxidation test. At last, the substrates were washed by ultrasonic cleaner and dried in air.

3.3 Coating

The propose of coating was to form a thin (nano level), uniform and non-agglomerated CeO_2 film on the SS 316L substrates. In this study, dip coating was chosen to be the coating method by using a slide motor. A coated substrate was hung on a frame, with elevating or descending the CeO_2 solution referred above, the substrate was immersed and then removed from the CeO_2 solution. The dipping speed was controlled to be 0.05mm/second. The residual solution on the substrate dried quickly in the air and CeO_2 film was formed. The repeating of this process with multiple immersion / removal cycles could increase the thickness of film coating.

Comparing with manual dip coating, this improved coating by using slide motor could provide a slow and constant motion. This has great benefit on uniformity of coating film and the agglomeration degree. Besides, the coating process was much more controllable on film thickness and agglomeration size.

3.4 High temperature oxidation test and Thermogravimetric Analysis (TGA) system

The weight of substrate would increase when the metal was oxidized, so it was a effective way by measuring the weight increasing to evaluate the oxidation degree. To record the kinetic weight change, the high temperature oxidation tests were performend in a TGA system. Twelve samples at different temperatures and different coating states were tested in 2 atmospheres: dry air and combustion atmosphere. The combustion atmosphere was the chemical products of CH_4 burning in dry air. The composition of combustion atmosphere included N_2, O_2 , H_2O, CO_2 and other component in the air.

Generally, water vapor present in an exhaust steam is easily condensed somewhere on the tubes or devices. So in this study, the CH_4 was ignited and burned directly in the TGA system to obtain the whole composition. A special gas inlet port was used for CH_4 burning and will be discussed in result section.

Oxidation tests in dry air were 5 hours and in combustion atmosphere were 120 hours. Because the oxidation in dry air was a simple reaction and that in combustion atmosphere had several stages and must be explained by more than one mechanisms.

3.5 X-ray diffraction (XRD) characterization

XRD technique was used to characterize the dried CeO_2 nanoparticles and the samples after oxidation. The possible existence of substances can be determined according to the XRD spectrum. XRD was performed using a Bruker D8 Discover with Cu K-alpha radiation. Scans were generally made from 20 to 70 degrees two theta with a scan rate of 2 degrees two theta per minute. The crystal size of CeO_2 nanoparticles was also estimated by using by Scherrer Equation .

3.6 Transmission Electron Microscope (TEM) characterization

TEM technique was used to measure the size of CeO_2 nanoparticles because other characterizations (XRD and SEM) could not accurately measure the size of particles that small. The ceria was dipped on the holder and dried at room temperature.

3.7 Scanning Electron Microscopy (SEM) characterization

SEM technique was used to observe the coating film on SS 316L substrates before oxidation and surface/cross section of oxidized samples. The SEM photos could reveal the agglomeration state of coating film and the morphology of oxidation structures. The SEM used in this study was a TopCon SM-300 and the operating voltages ranged from 5kv-10kv.

4 Experimental results

4.1 Synthesis of ceria nanoparticles

In this research, ceria nanoparticles were prepared by the microemulsion method. The earlier study has proved that non-agglomerated ceria nanoparticles can be efficiently synthesized by means of the microemulsion method [1]. And here, we further improved the previous method to get a long-term stable ceria nanoparticles.

The details of synthesis steps are listed below:

1) 4.446g AOT was dissolved in 100 ml toluene to form a 0.1 mol/L AOT in toluene solution.
2) 0.0434g $Ce(NO_3)\cdot 6H_2O$ was dissolved in 10 ml distilled water to form a 0.1 mol/L aqueous solution.
3) 1.67 ml ammonium hydroxide was dissolved in distilled water to form a 10 ml 5% w/w dilute aqueous ammonia solution.
4) $Ce(NO_3)\cdot 6H_2O$ aqueous solution in step (2) was added dropwise into toluene solution in step (1). The toluene was stirred by magnetic stirrer during the addition.
5) The mixed solution in step (4) was stirred for 1 hour. The stirring speed here is a critical parameter and will be discussed later.
6) The dilute aqueous ammonia solution in step (3) was slowly added dropwise into the mixed solution in step (5). A speed of 12-15 drops per minute was maintained and the whole step (6) lasted for about 10 minutes.
7) The mixed solution in step (6) was stirred for 1 hour with a proper stirring speed and a pale brown emulsion was obtained
8) The emulsion in step (7) was allowed to stand for 30 minutes and the emulsion was

allowed to separate into 2 layers. The upper layer was toluene containing non-agglomerated ceria and AOT. The bottom layer was water containing ammonia and a small amount of cerium.

9) Not a agglomerated cerium layer or structure was observed by naked eye. The color of upper toluene layer became bright brown or yellow during the step. In this step, Ce^{3+} was oxidized to the $Ce(OH)_4$.

10) The upper layer of toluene with non-agglomerated ceria and AOT was extracted by transfer pipet. The solution was reserved in refrigerator which the temperature was a little above 0 °C. A lower temperature can slow down the further agglomeration of ceria and make a possibility for long-term storage. However, in step (9), the solution was not stable and the ceria precipitated in a few hours. Up to here, the non-agglomerated ceria nanoparticles had been made . The steps (10) to (12) were tried to remove the excess AOT and stabilize the ceria in the solution.

11) The toluene solution stored in refrigerator (little above 0 °C) for 12 hours and due to the precipitation the solution was divided into two parts by gravity. The upper layer was toluene and AOT, almost transparent. The bottom layer was precipitation ceria with toluene and AOT, light yellow. The upper layer was removed and the rest solution was refilled with pure toluene to the same volume. New solution was stirred for 5 minutes. Through this step, the concentration of AOT was reduced without hurting that of ceria. However, the ceria did not precipitate as solid. Actually, the precipitation of ceria much more like a liquid separation: the precipitation occupied a considerable part of the volume, usually was 1/3 or 1/4. This volume could be kept for a time and further volume

reduction was very slow. So an assumption can be made that ceria nanoparticles formed an unstable agglomeration with AOT. This special agglomeration made the ceria still soluble in the toluene and prevent the further agglomeration. What is more important, ultrasonic treatment can destory this special agglomeration and cause the ceria re-dispersed in solution with tiny particles.

12) It should be noted that the AOT was not averagely distributed into two layers in step (10). More AOT was distributed into the bottom layer because part of AOT participated in the formation of the sol. So only a small amount of AOT is removed in a single dilution operation. On the other hand, the dilution of AOT could remove the AOT that adsorbed on the ceria, which played a critical role on anti-agglomeration. Because of the reasons above, appropriate repetition of step (10) was required and in this research the step (10) was repeated for 5 times to obtain an acceptable AOT level in ceria product.

13) After several repetitions of step (10), most of AOT had been removed. Then the solution was treated by ultrasonic treatment for 5 min. The ceria after ultrasonic treatment became stable and no longer precipitated. In this research, all the coated tests were based on the same set of ceria samples and no obvious separation or precipitation was recorded for more than 6 months.

4.1.1 The relationship between stirring speed and agglomeration degree

The agglomeration degree of ceria nanoparticles has great impact on high temperature oxidation resistant performance. Several factors were studied in the synthesis such as stirring speed, temperature, stirring time, and the amount of chemistry reagent. The result showed that stirring speed had much more significant effect than any other factors on the agglomeration degree.

The magnetic stirring was used widely in the whole synthesis process: mixing of toluene solution and $Ce(NO_3)\cdot 6H_2O$ aqueous solution (step 4 and 5), mixing of toluene solution and dilute aqueous ammonia (step 6 and 7), stirring of refilled solution (step 9 and 10). Here, long time stirring are discussed to reveal how stirring speed influence the ceria synthesis.

In the test the stirring speed was set at sample A: 300 rpm (revolutions per minute), sample B: 500 rpm and sample C: 700 rpm respectively. Figure 5 shows the solution just after stirring with $NH_4(OH)$ for 30 minutes (step 8).

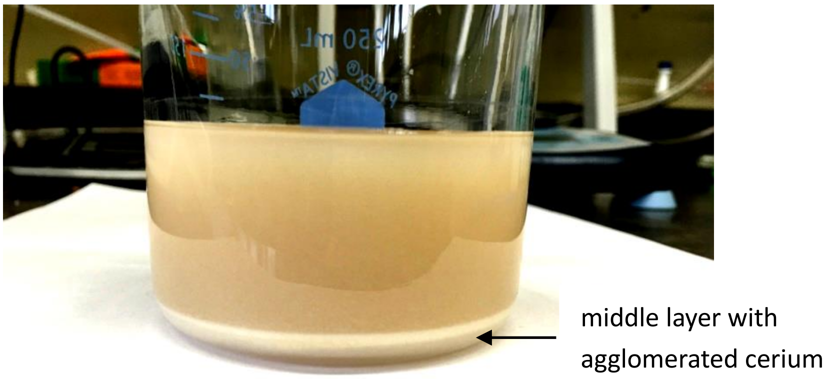

A, 300 rpm

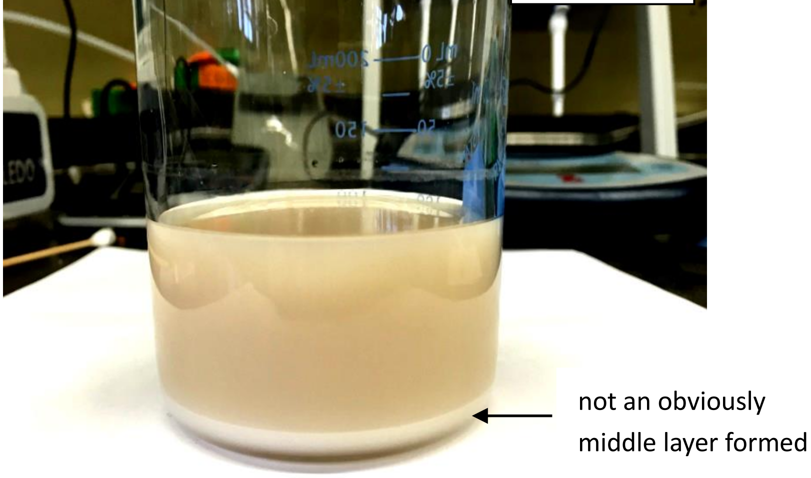

B, 500 rpm

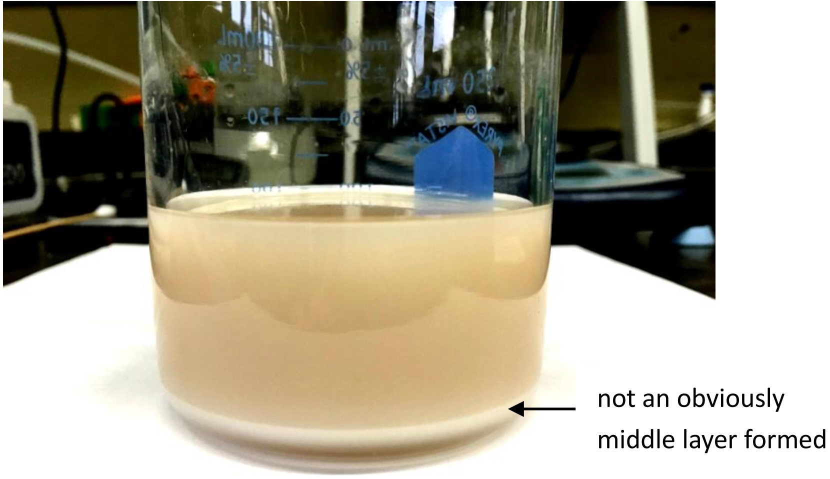

C, 700 rpm

Figure 5, 3 minutes after stirring with $NH_4(OH)$, the speed of sample A, B and C were 300 rpm/500 rpm /700 rpm respectively.

All three samples looked similar as the toluene phase and water phase separated quickly. The upper layer was toluene with $Ce(OH)_4$ and AOT. The color of pure $Ce(OH)_4$ should be bright brown but in this stage it was pale because of surrounding of AOT. Part of AOT was distributed into the water phase so the bottom layer looked white. The only difference can be figured out was a middle layer forming in sample of 300 rpm. This middle layer was agglomerated $Ce(OH)_4$ with large amount of AOT.

Figure 6 shows the solution after 30 minutes standing. Sample B of 500 rpm and C of 700 rpm had no significantly change. However for the sample A, almost all the cerium agglomerated and precipitated. Part of cerium was pushed into the water phase due to the gravity. The middle layer disappeared and the boundary of toluene phase and water phase was blurry. Then the toluene part was extracted as much as possible and stood for another 12 hours in refrigerator which was referred in step 9.

Figure 7 shows the upper layer after another 12 hours standing in refrigerator. The sample A at 300 rpm revealed the further volume reduction of cerium part. All the cerium was gathered at the bottom of the beaker which only occupied a very thin brown layer. Some AOT adhered to the surface of cerium layer. In this stage, the form of element cerium changed from $Ce(OH)_4$ to CeO_2 and the color of cerium also changed from brown to yellow or bright yellow. To the sample B at 500 rpm, the transformation of $Ce(OH)_4$ proceed faster. All the cerium part appeared as a bright yellow. What more important was the precipitation seems didn't occur completely and it stopped somewhere in the middle. From the figure cerium part occupied about 2/3 of the whole volume. However in the sample C, the precipitation of cerium did not happen at all. As well as that in the sample B, the most

$Ce(OH)_4$ transformed to CeO_2 . Because of the maintain of single layer, the AOT can't be diluted by exchanging upper AOT rich layer, so the test of sample stopped in this stage but sample A and B finished the AOT diluting process (step 11 and 12).

Figure 8 shows sample A at 300 rpm and sample B at 500 rpm after finishing the AOT diluting by 5 repetition of exchanging process. All the $Ce(OH)_4$ had transformed to CeO_2 for both 300 and 500 rpm. The difference between each samples was the precipitation or the agglomeration state. In sample A, the precipitation still occupied a small volume and the appeared as a solid phase. For the sample B, the precipitation occupied about 2/5 of the whole volume and appeared as a liquid phase.

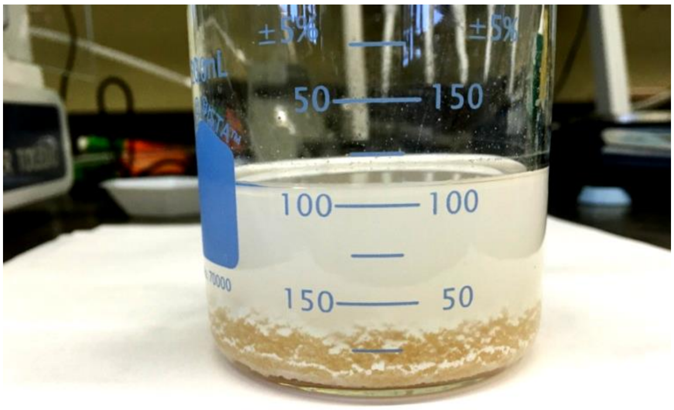

A, 300 rpm

B, 500 rpm

C, 700 rpm

Figure 6, 30 minutes after stirring with $NH_4(OH)$, the speed of sample A, B and C were 300 rpm, 500 rpm, 700 rpm respectively.

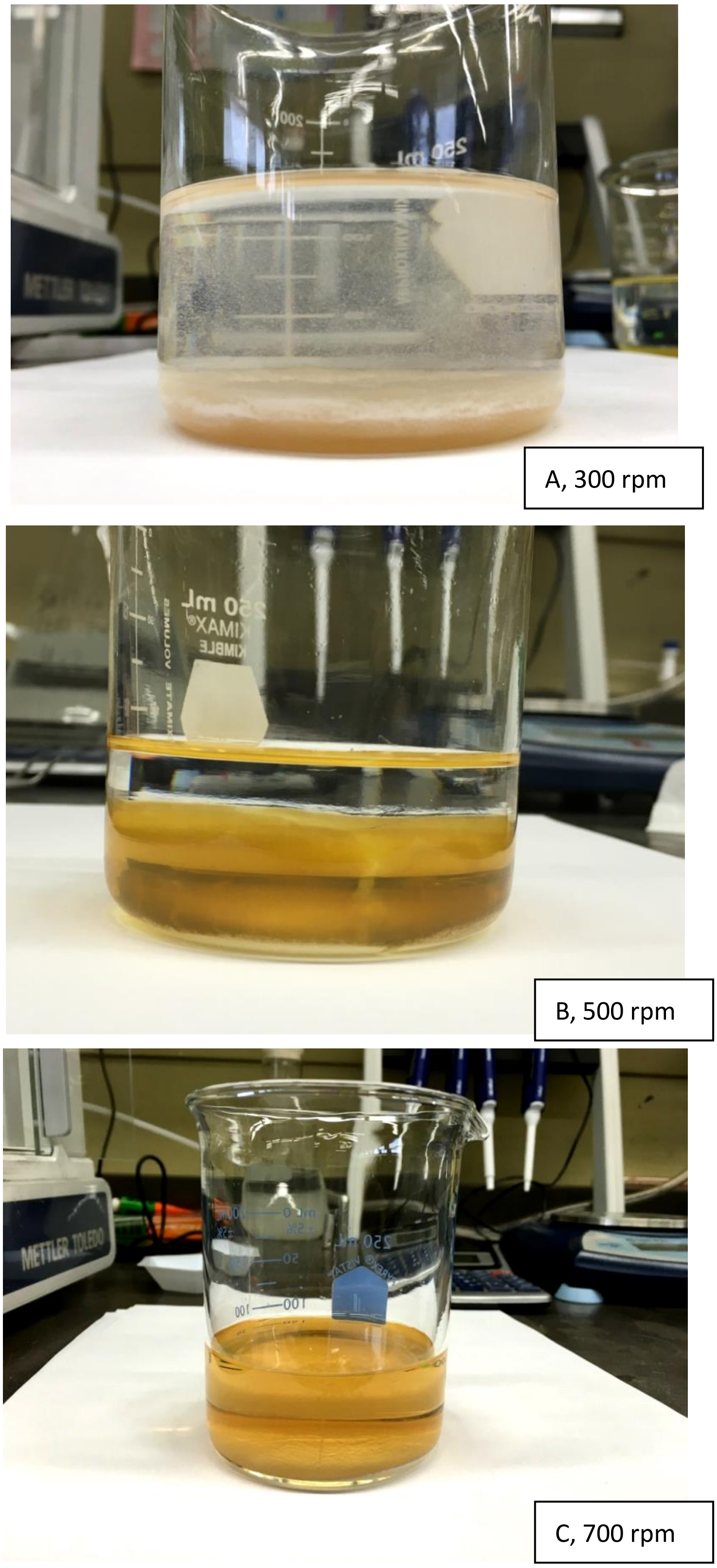

A, 300 rpm

B, 500 rpm

C, 700 rpm

Figure 7, upper layer, 12 hours after stirring with $NH_4(OH)$, the speed of sample A, B and C were 300 rpm, 500 rpm, 700 rpm respectively.

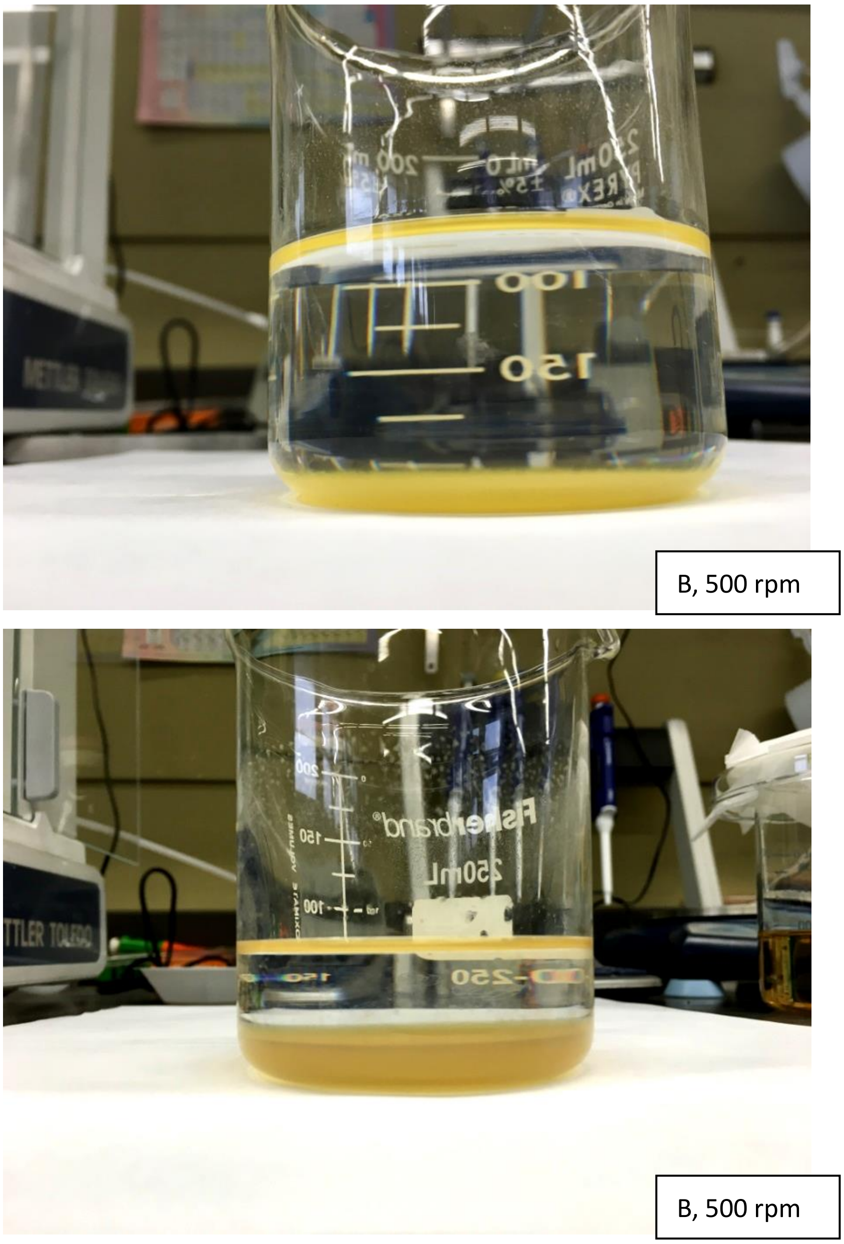

Figure 8, upper layer, after diluting the AOT for 5 times, the speed of sample A, B and were 300 rpm,500 rpm respectively.

In summary, stirring speed had a significant influence on the ceria synthesis. This influence was mainly reflected by the degree of agglomeration and precipitation. A higher stirring speed could cause less agglomeration and less precipitation. We can assume that the overall cerium compound particle size and the precipitation have a positive correlation. So the conclusion is that the stirring speed affects the initial particle size or the agglomeration degree. Lower stirring speed cause larger initial size or serious agglomeration. The cerium compound can remain at a small size the stirring speed is high enough. However, an excess stirring speed can prevent the layering of the solution which means the diluting of AOT is impossible in this synthesis method. In this synthesis, a moderate stirring speed is required and according to the test this speed can be 500 rpm. If we can separate the AOT from cerium compound in a homogeneous solution without hurting the separation of the ceria nanoparticles, in that case a higher stirring speed is preferred.

4.1.2 X ray diffraction

The toluene in prepared solution was evaporated at 60 °C and the ceria nanoparticels were collected for characterization. Figure 9 shows the XRD spectrum of dried ceria nanoparticles. Peaks of $Ce(OH)_4$ or AOT were not found in the spectrum. Four main peaks of CeO_2 were marked in the spectrum.

The crystal size of ceria was calculated by Scherrer Equation:

$$\tau = \frac{K\lambda}{\beta\cos\theta}$$

where K is the shape factor, λ is the X ray wavelength, β is the full width for the half maximum intensity for the peak (FMHM) and ϑ is the Bragg angle and τ is mean size.

Here the (111) peak was used to calculated the crystal size, the 2ϑ of peak (111) was 28.6^o and cosθ was 0.969. The shape factor K was 0.9 and the λ was 0.15418 nm. According to the figure, the FMHM was about $3\text{-}3.5^o$ or 0.0523-0.0611 radians. So the main crystal size was about 2.34-2.73 nm by XRD spectrum.

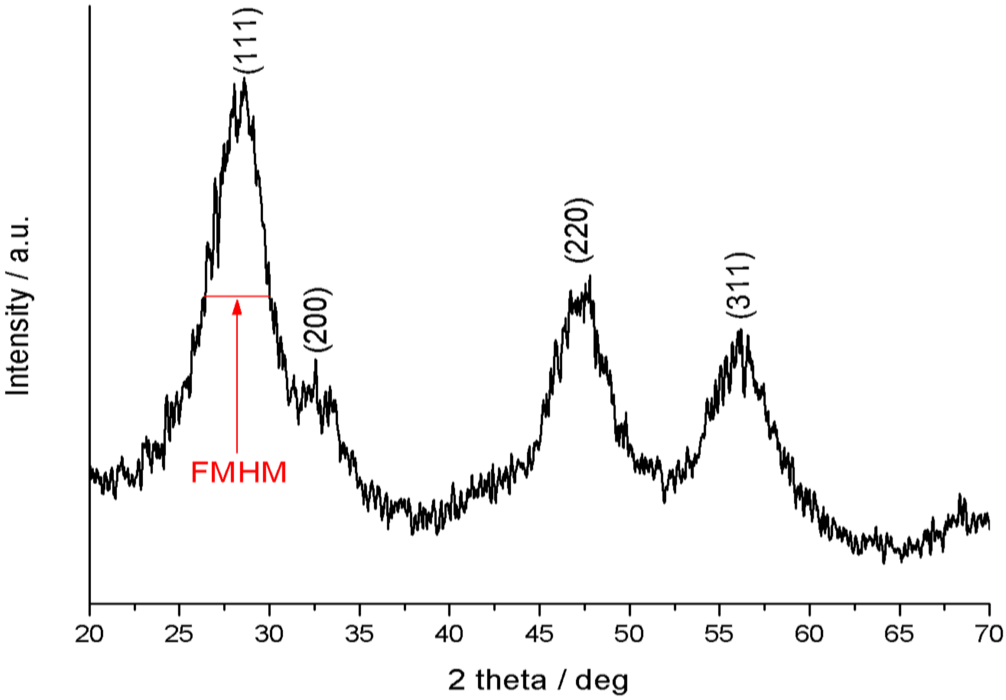

Figure 9, XRD spectrum of the dried ceria nanoparticles.

4.1.3 Transmission Electron Microscope.

Figure 10 shows the TEM micrographs of dried ceria (CeO_2) nanoparticles. The test sample was dipped on the substrate and dried at room temperature. Figure 10-b clearly shows the particle size of CeO_2 was about 2-4 in diameter, the result of TEM basically consist with that of XRD analysis. In figure 10-a, CeO_2 nanoparticles were agglomerated. However, by analyzing the morphology of agglomeration, we have enough reasons to believe that the agglomeration was formed during the drying on substrate rather than in the solution. Firstly, the brightness of particles were uniform in figure 10-a. Not a particular bright or dark zone was found in the figure-a. This means the thickness of the whole agglomeration was similar and the thickness itself was pretty small. If the agglomeration was formed in the solution, the general morphology should be a dark spherical center and bright surrounding. Secondly, the morphology of agglomeration has complex net structure, which means this was not a possible structure in the solution. In summary, we think the possible mechanism of the agglomeration in TEM is the particle flowing with the liquid, colliding and stopped by other particles during the drying. Even though the agglomeration was formed in the solution, the agglomeration size should be much smaller than the structure in the figure 10-a.

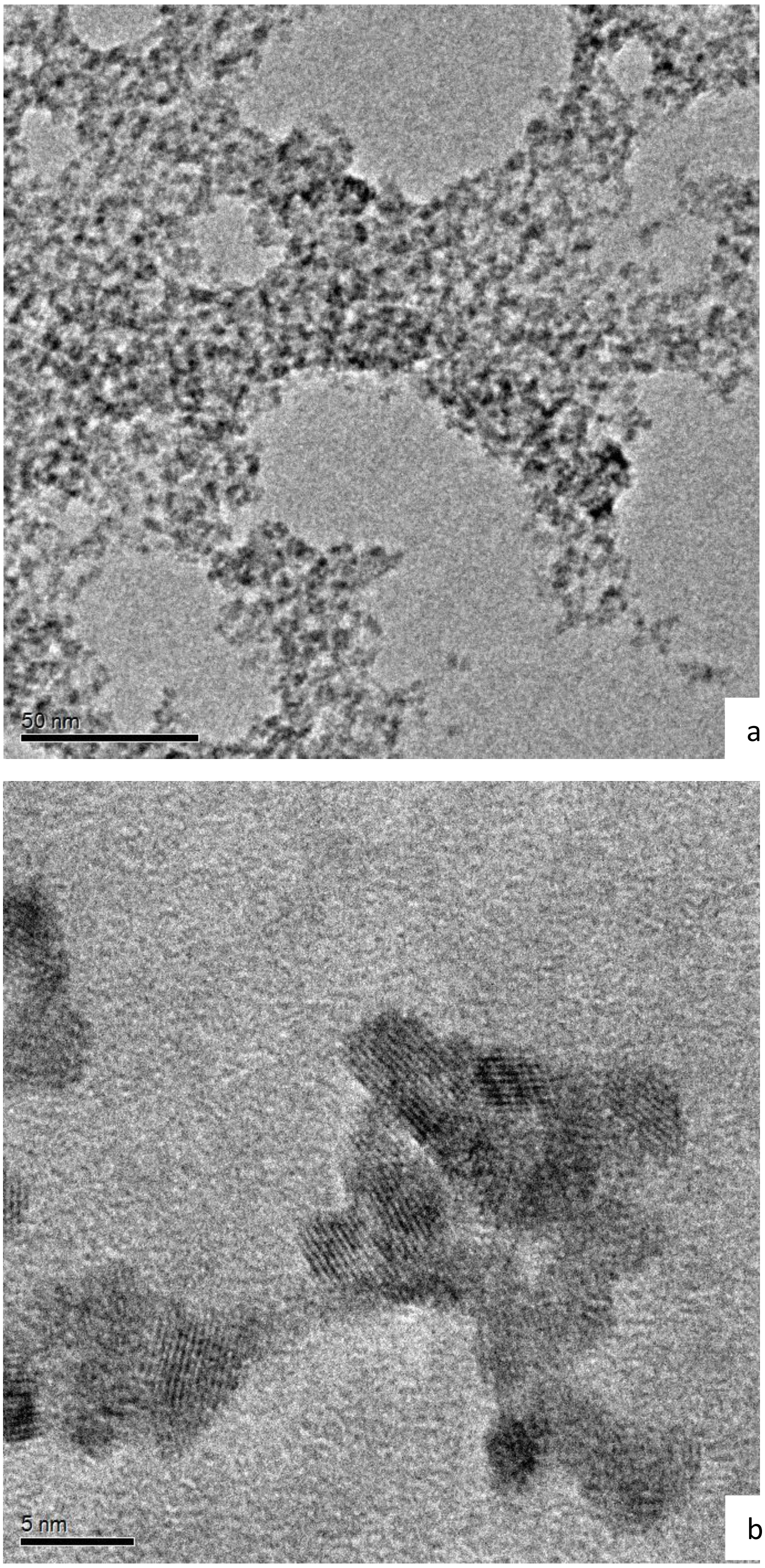

Figure 10 , TEM micrographs of CeO_2 nanoparticles, dipped on the holder and dried at room temperature.

4.2 Substrate preparation and coating.

4.2.1 Substrate preparation

The 316L austenitic stainless steels were purchased from Speedy Metals with the thickness of 0.03 inch (0.76mm). The samples were cut into slices of 20mm x 10mm x 0.76mm. Then the samples were grinded by 1000 SiC sand paper and the thickness was reduced to about 0.58-0.62mm. Two holes were punched on the samples for hanging and at last the samples were washed by ultrasonic cleaner for 5 minutes. Figure 11 shows the samples before and after the preparation.

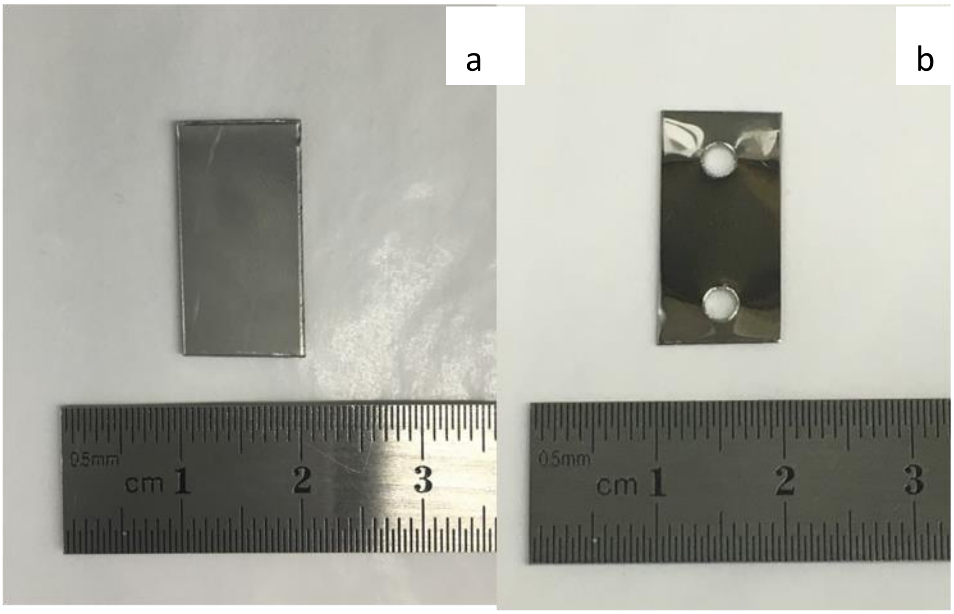

Figure 11, stainless steel 316L samples before (a) and after (b) the preparation.

4.2.2 Coating procedure

Dip coating method was chosen to apply the combination of CeO_2 and SS 316L substrates. In the experiment, a slide motor was introduced to overcome instability of manual operation. Figure 12 shows the slide motor and its fixing on the frame.

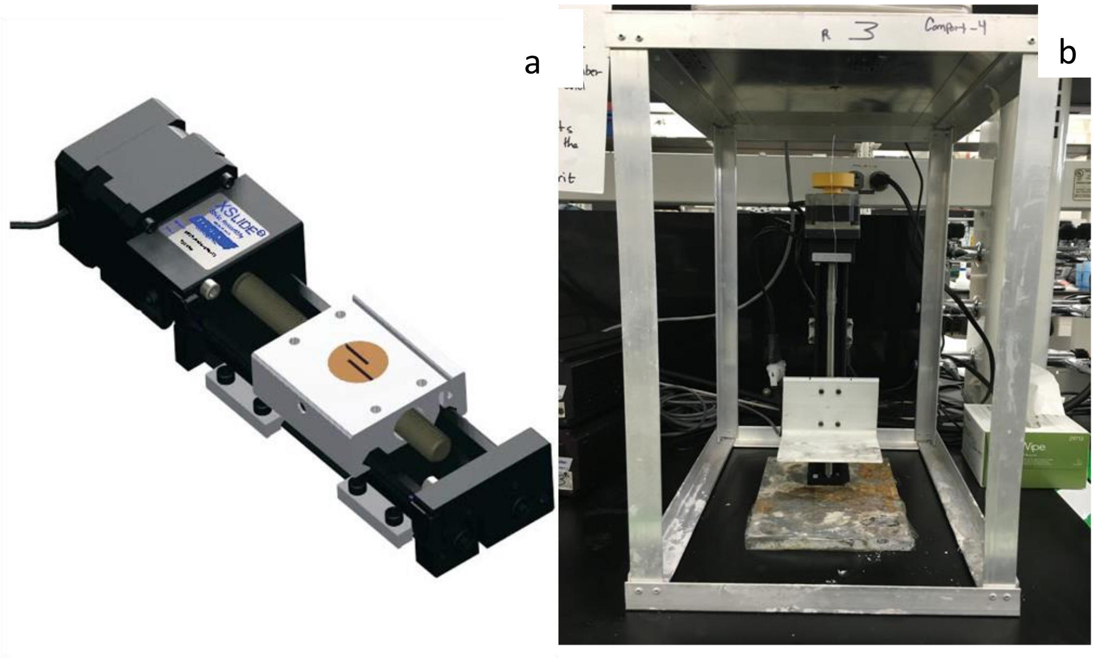

Figure 12, Slide motor used for coating (a) and its fixing on the frame (b).

In the coating procedure, the SS 316L substrate was hung on the hook above and keep static. Slide motor drove the breaker to achieve relative motion between substrate and coating materials. The following is a detailed operation process: Vertically hung SS 316 substrate was immerged into the coating solution at the speed of 0.05mm/second. Then the substrate was elevated from the solution at the same speed after 1 minute suspension. By using the high volatility of toluene, the dip coating dried rapidly after leaving the solution.

Repeating of operation above could increase the thickness of coating layer.

Through this method, the traditional dip coating received a considerable improvement. Firstly, the thickness of coating layer was more uniform and controllable. The constant elevating speed made same amount of solution adhering on the substrate and the coating layer remain a highly uniform except upper and lower ends. By controlling the speed and repeating times the thickness of the coating could be controlled reliably. Secondly, a dynamic and transient drying could reduce the secondary agglomeration during the liquid evaporation.

In this experiment, the coating layer was very thin and there was no visible difference between coated and uncoated sample by naked eye so the regular photographs were not showed. Figure 13 shows the SEM micrographs of CeO_2 film coated on the SS 316L substrate. At lower magnification (A and B), the bright area was the coating film and the dark area was uncoated part or very thin coated. From the figure, most part of surface was coated and the uncoated part was less than 10% of the whole surface. Some large agglomerated particles about 2-3μm can be founded in figure 9-B. In figure 9-C, the fewer agglomerated particles were distributed on the substrate uniformly. The average size of these particles were about 50-100 nm.

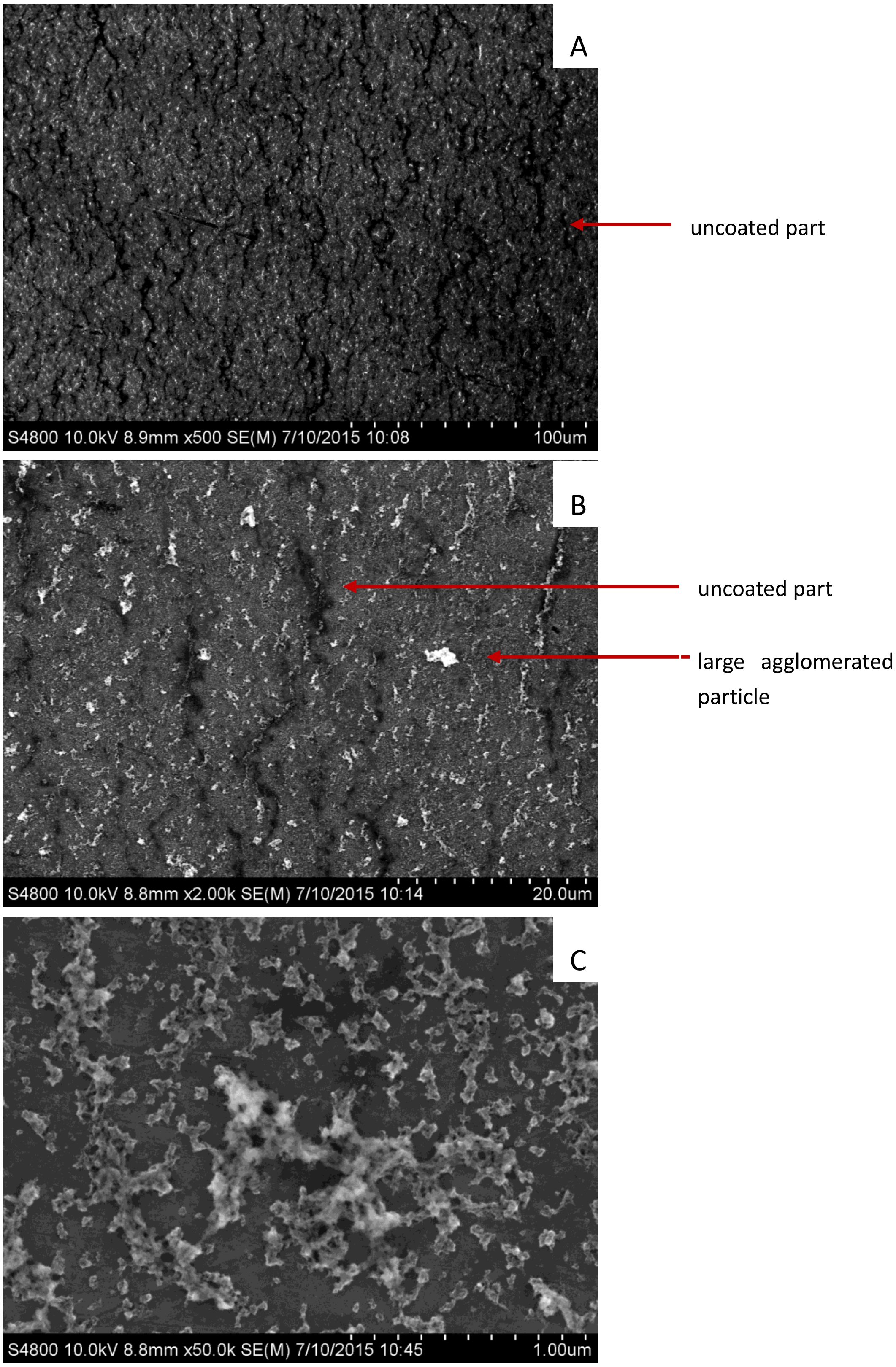

Figure 13, SEM micrographs of CeO_2 film coated on the SS 316L substrate. A,B and C were x500, x2000 and x50000 magnification respectively.

4.3 High temperature oxidation

4.3.1 Thermogravimetric Analysis System

All the oxidation tests were performed in a custom thermogravimetric analysis (TGA) system. Figure 14 shows the schematic diagram of the TGA system used in this study. Figure 15 shows a photograph of the TGA system.

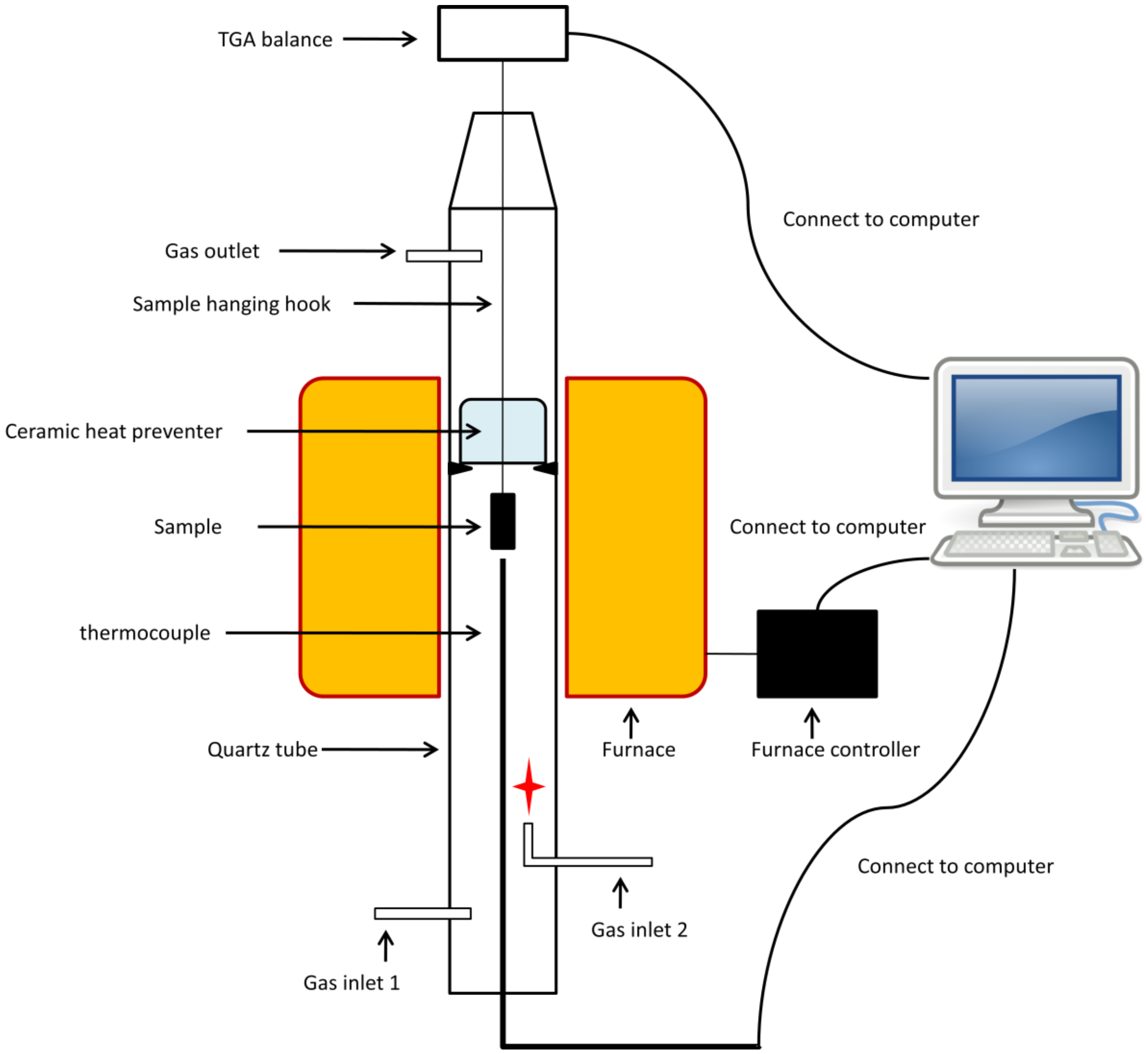

Figure 14, the schematic diagram of the TGA system

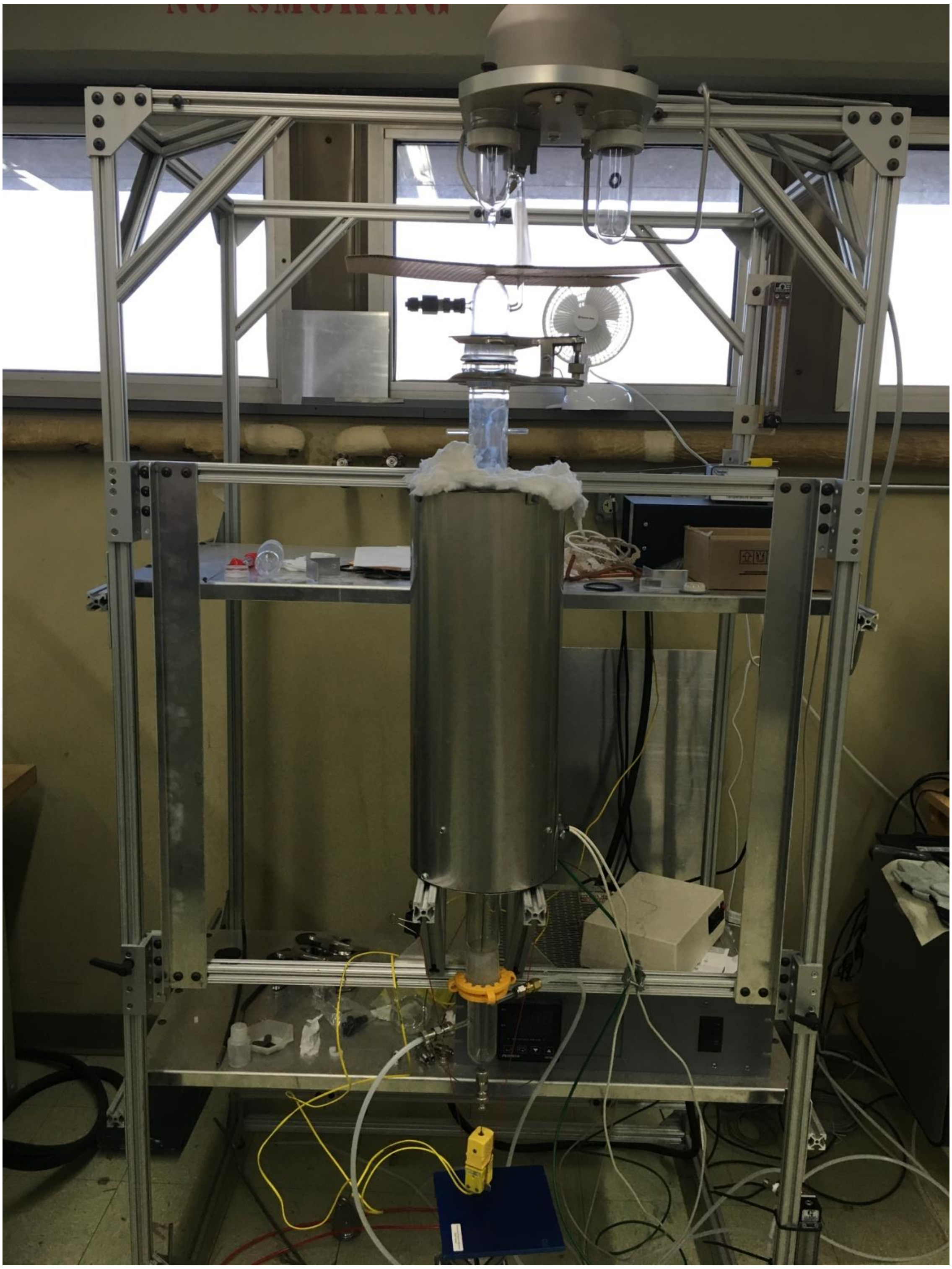

Figure 15, photograph of the TGA system.

The thermogravimetric analysis system consisted of software and hardware part. All the software part including furnace controlling, balance controlling and data display was controlled by computer directly. The main parts of hardware were:

1) A 7 digits sensitivity microbalance at the top of the system.
2) High temperature tube furnace of type Thermolyne 54500.
3) Quartz tube and ceramic heat preventer
4) Ni-Cr sample hanging hook.
5) A thermocouple for temperature detecting and controlling.

There were two gas inlets and one gas outlet on the quartz tube. Gas inlet 1 was used for dry air input and Gas inlet 2 with a turning was used for flammable gas. Flammable gas could be ignited at the exit of gas inlet 2 and a stable flame maintained. The sample was suspended by a sample hanging hook with no touching with any part in the quartz tube except the balance mechanism. The ceramic heat preventer could slow down the air/heat flow which would interfere with the balance.

4.3.2 Oxidation atmosphere.

Two series of SS 316L samples were oxidized in two different atmospheres: dry air and combustion gas.

The composition of dry air is shown in table 2.

Component	N_2	O_2	Ar	CO2	Ne	He
Volume (%)	78.084	20.947	0.934	0.033	0.00182	0.00052

Table 2, the composition of dry air

In the dry air, 6 samples were tested at temperature 800°C, 850°C and 900°C for both coated and uncoated situation. The gas flow was set at 60 cm^3/min.

The combustion gas atmosphere was the combustion mixture of dry air and pure methane (CH_4) at the ratio of 40:1, which the gas flow was set at 800 cm^3/min and 20 cm^3/min respectively. The minimum CH_4 flow to maintain a stable flame was about 10-12 cm^3/min. The reaction equation of CH_4 burning in the air and the ratio of each components are listed below:

$$\mathrm{CH_4 + 2O_2 = CO_2 + 2H_2O}$$

$$1 \quad : \quad 2 \quad : \quad 1 \quad : \quad 2$$

And the overall reaction (the ratio of oxygen in the dry air was approximated to 20%) :

$$\mathrm{32N_2 + 8O_2 + CH_4 = 32N_2 + 6O_2 + CO_2 + 2H_2O}$$

$$32 \quad : \quad 8 \quad : \quad 1 \quad : \quad 32 \quad : \quad 6 \quad : \quad 1 \quad : \quad 2$$

The content of each components after burning was: N_2 78.0%, O_2 14.6%, CO_2 2.43% and H_2O 4.88%. The content of oxygen decreased more than 25% and carbon dioxide with vapor were introduced. The humidity of the mixture gas was about 5%. The test temperature was set at 650°C, 750°C and 850°C and no condensation was found around the test samples during the test operation. Most water vapor was maintained in the gas phase inside the quartz tube and a small amount was condensed on the gas outlet tube.

4.3.3 TGA kinetics data of high temperature oxidation

Twelve samples divided into two groups were oxidized by TGA system and the kinetic mass data was recorded. Each sample was oxidized for 5 hours in dry air or 120 hours in combustion gas. Table 3 shows the oxidation conditions for these 12 samples. In the earlier work, the coating was found to provide no help in combustion atmosphere when the temperature was above 800°C. Both coated and uncoated samples had very serious oxidation. Therefore the test temperature for combustion atmosphere was lower and set in the range of 650°C -850°C. However in dry air, the oxidation was rather faint when the temperature was lower than 750°C and sometimes could not be effectively recorded by the TGA balance. Therefore the test temperature for dry air was higher from 800°C -900°C. That is the reason of inconformity of the two groups test temperatures.

Coating state	uncoated	coated
Dry air	800°C /850°C /900°C	800°C /850°C /900°C
Combustion gas	650°C /750°C /850°C	650°C /750°C /850°C

Table 3, test conditions for all 12 oxidation test, grouped by atmosphere or coating state.

Figure 16 -18 shows isothermal oxidation kinetic plots and parabolic trend line of uncoated and coated SS 316L at 800 °C, 850°C, 900°C in dry air respectively.

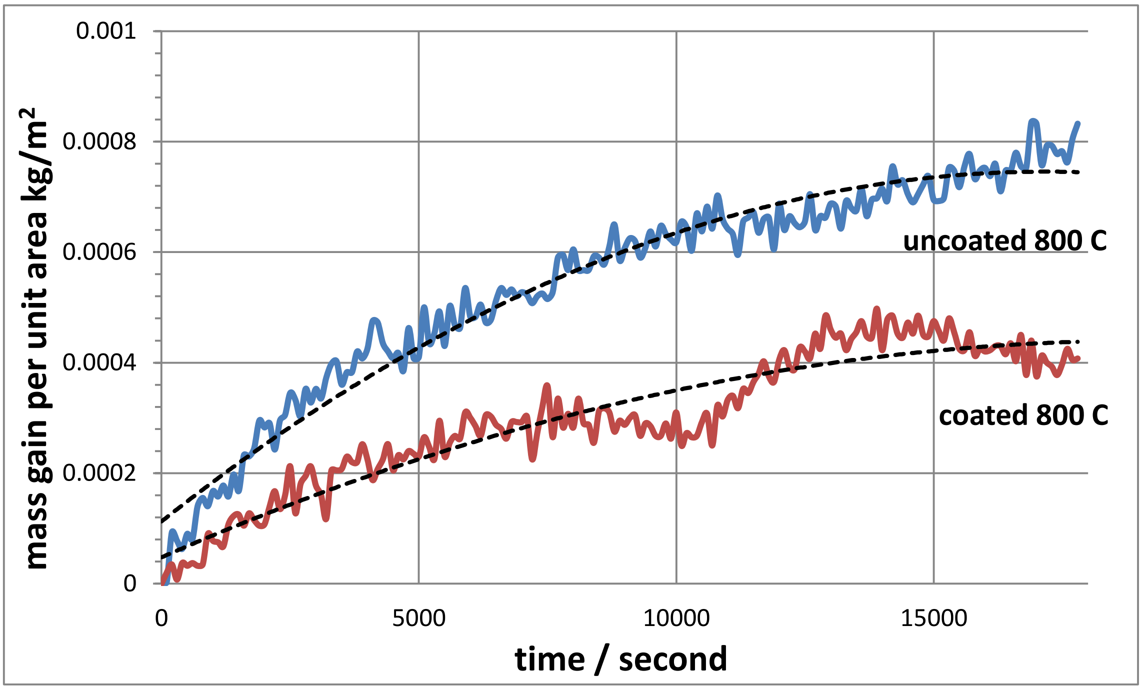

Figure 16 Isothermal oxidation kinetic plots and parabolic trend line of uncoated and coated SS 316L at 800 °C in dry air.

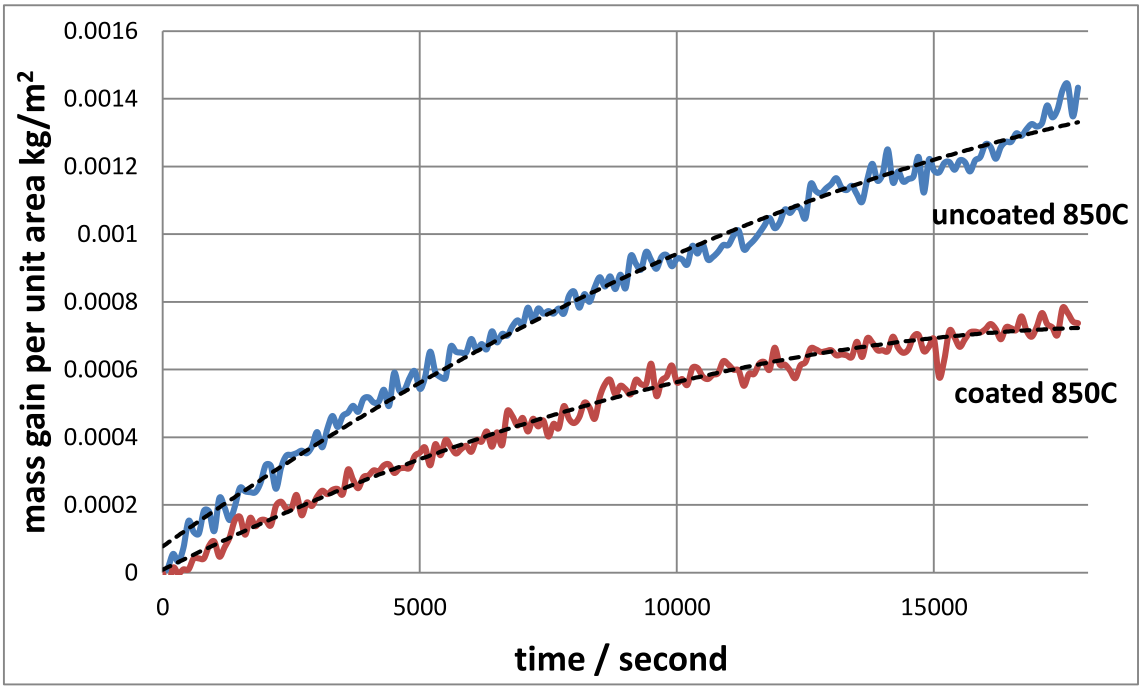

Figure 17, Isothermal oxidation kinetic plots and parabolic trend line of uncoated and coated SS 316L at 850 °C in dry air.

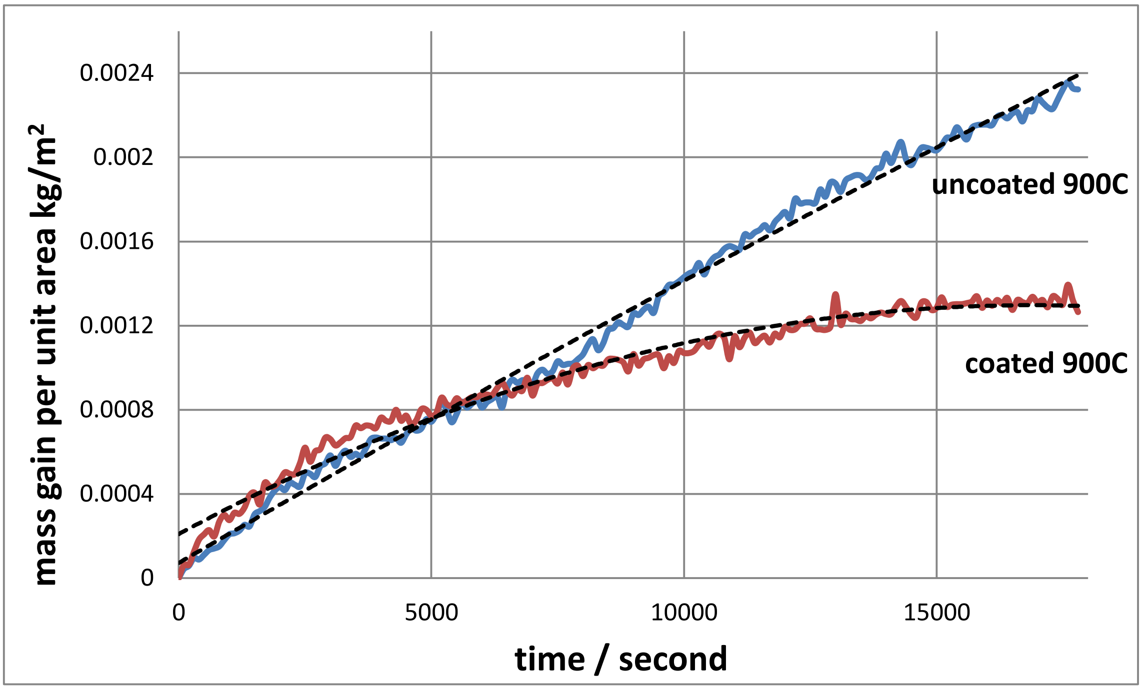

Figure 18, Isothermal oxidation kinetic plots and parabolic trend line of uncoated and coated SS 316L at 900 °C in dry air.

Figure 19 shows isothermal oxidation kinetic plots and parabolic trend line of uncoated SS 316L at different temperature in dry air. Figure 20 shows isothermal oxidation kinetic plots and parabolic trend line of coated SS 316L at different temperature in dry air. Figure 21 shows the oxidation rate constant K_p (first term coefficient of trend line)for the uncoated samples in dry air. Figure 22 shows the oxidation rate constant K_p (first term coefficient of trend line)for the coated samples in dry air. Table shows the oxidation rate constant K_p for both coated and uncoated samples.

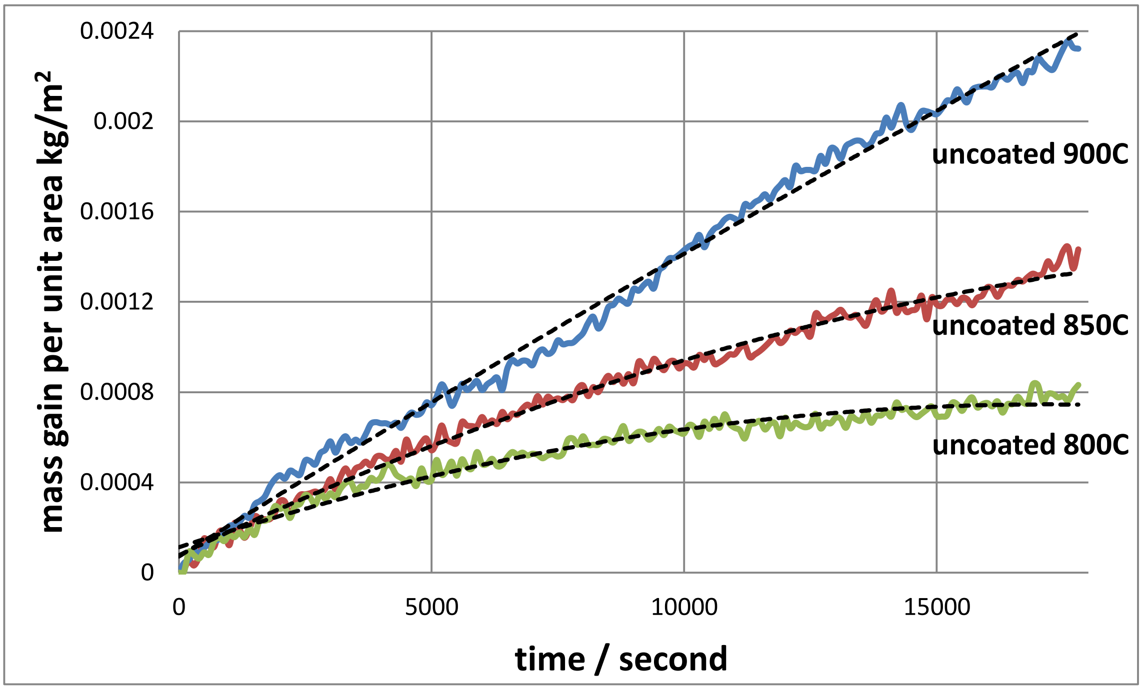

Figure 19, Isothermal oxidation kinetic plots and parabolic trend line of uncoated SS 316L at different temperature in dry air.

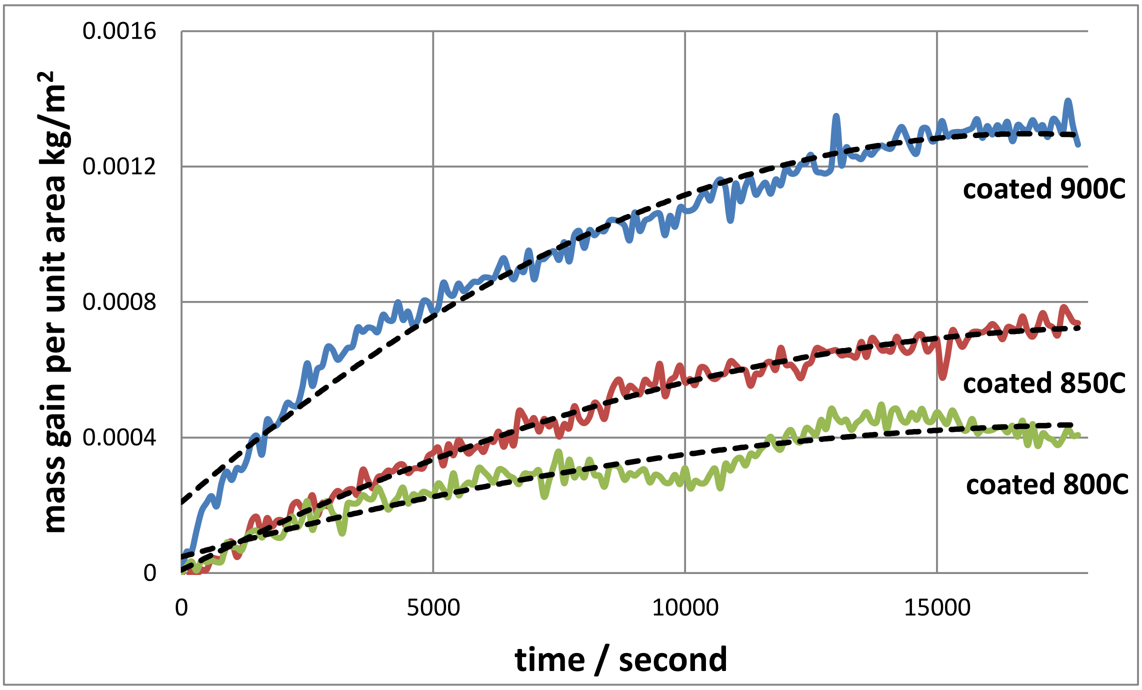

Figure 20, Isothermal oxidation kinetic plots and parabolic trend line of coated SS 316L at different temperature in dry air.

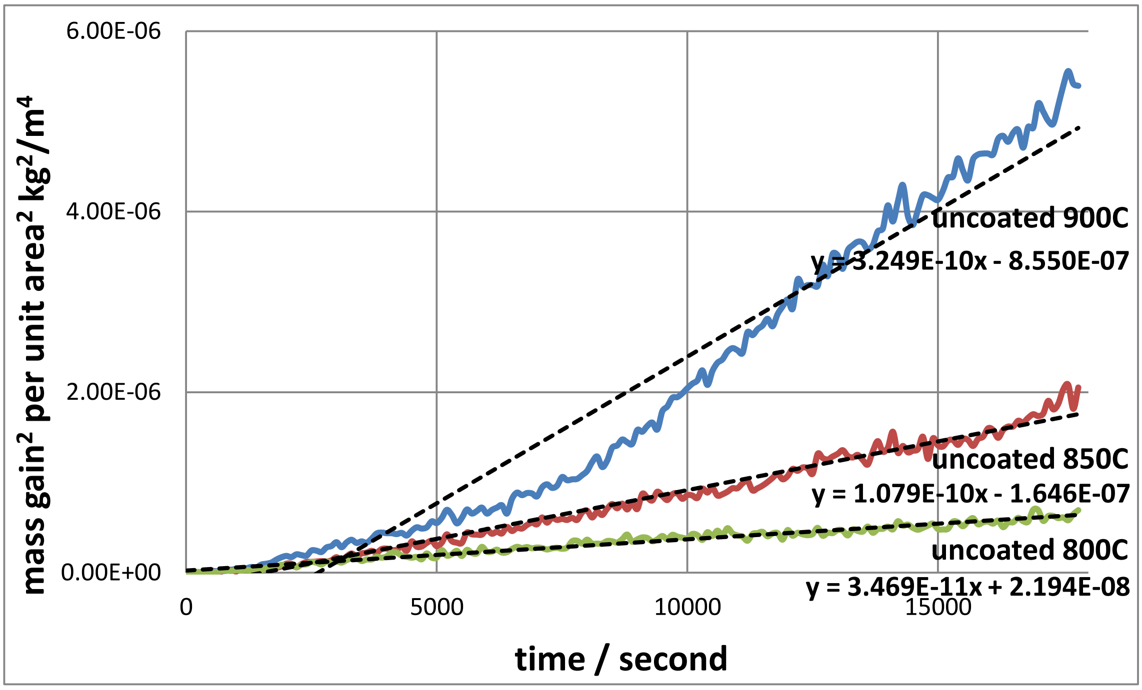

Figure 21, Oxidation rate constant K_p (first term coefficient of trend line)for the uncoated samples in dry air.

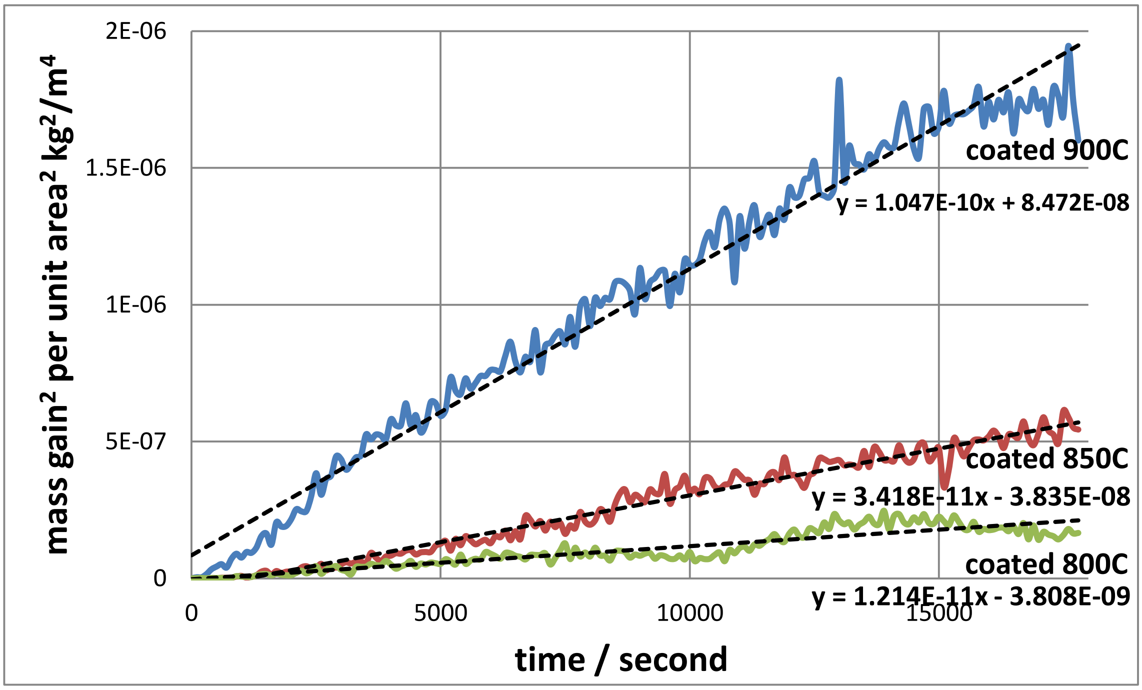

Figure 22, Oxidation rate constant K_p (first term coefficient of trend line)for the coated samples in dry air.

Oxidation rate constant K_p $(kg^2/m^4)/s$	800 °C	850°C	900 °C
uncoated	3.469×10^{-11}	1.079×10^{-10}	3.249×10^{-10}
coated	1.214×10^{-11}	3.418×10^{-11}	1.047×10^{-10}

Table 4, Matrix of oxidation rate constant K_p of dry air oxidation.

At each temperature group, the mass gain of the coated sample was about half of that without coating from figure 16-18. Figure 19-20 revealed that the mass increase of the coated samples slowed significantly after 5 hours. On the contrary, the mass increase of the uncoated samples did not have a corresponding slowing. Furthermore, the acceleration difference was more observable in higher temperatures: In figure 18, the mass increasing rate of coated and uncoated sample was almost the same for the first 7000 seconds at 900 °C. After 7000 seconds, the mass increase rate of the coated sample gradually slowed down and the rate of uncoated sample almost stayed constant. Eventually, a considerable mass gain gap at 18000 seconds was obtained.

By analyzing figures 16-22 and their trend lines, the following conclusions were obtained: The cerium oxide coating was effective on SS 316L oxidation protection in dry air at the temperature range of 800 °C -900 °C. In a short term oxidation, coating provided similar protecting level by comparing the mass increasing gap. However, in long term oxidation, the coating would perform better in higher temperature due to the differences on both oxidation speed and oxidation acceleration.

Figure 23 -25 show isothermal oxidation kinetic plots and parabolic trend line of uncoated and coated SS 316L in combustion atmosphere at 650 °C,750 °C, 850 °C respectively. Figure 26-27 show isothermal oxidation kinetic plots and parabolic trend line at different temperature in combustion atmosphere, uncoated and coated respectively. Figure 28-29 show the oxidation rate constant K_p (first term coefficient of trend line) in combustion atmosphere, uncoated and coated respectively.

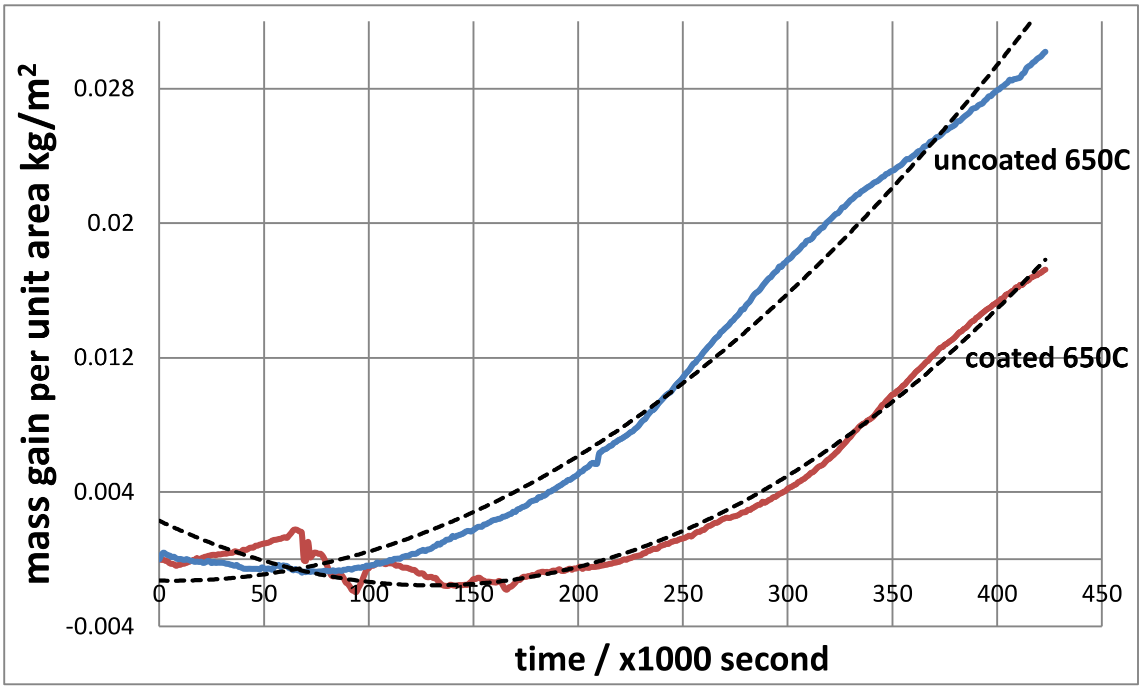

Figure 23, Isothermal oxidation kinetic plots and parabolic trend line of uncoated and coated SS 316L at 650°C in combustion atmosphere.

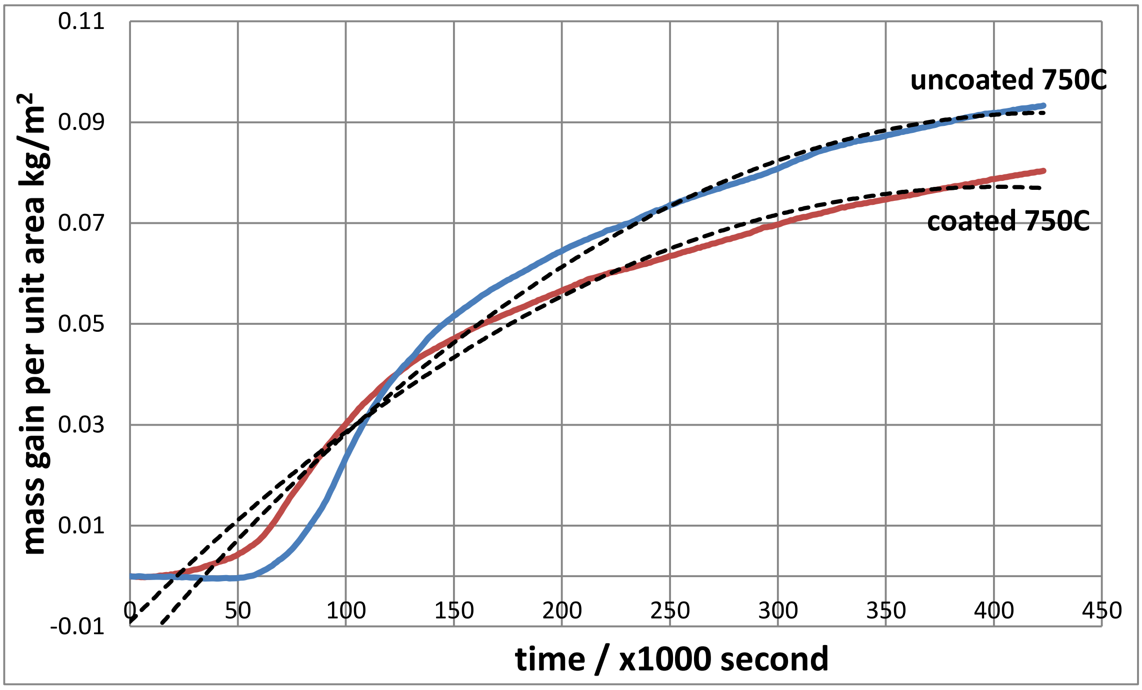

Figure 24, Isothermal oxidation kinetic plots and parabolic trend line of uncoated and coated SS 316L at 750 °C in combustion atmosphere

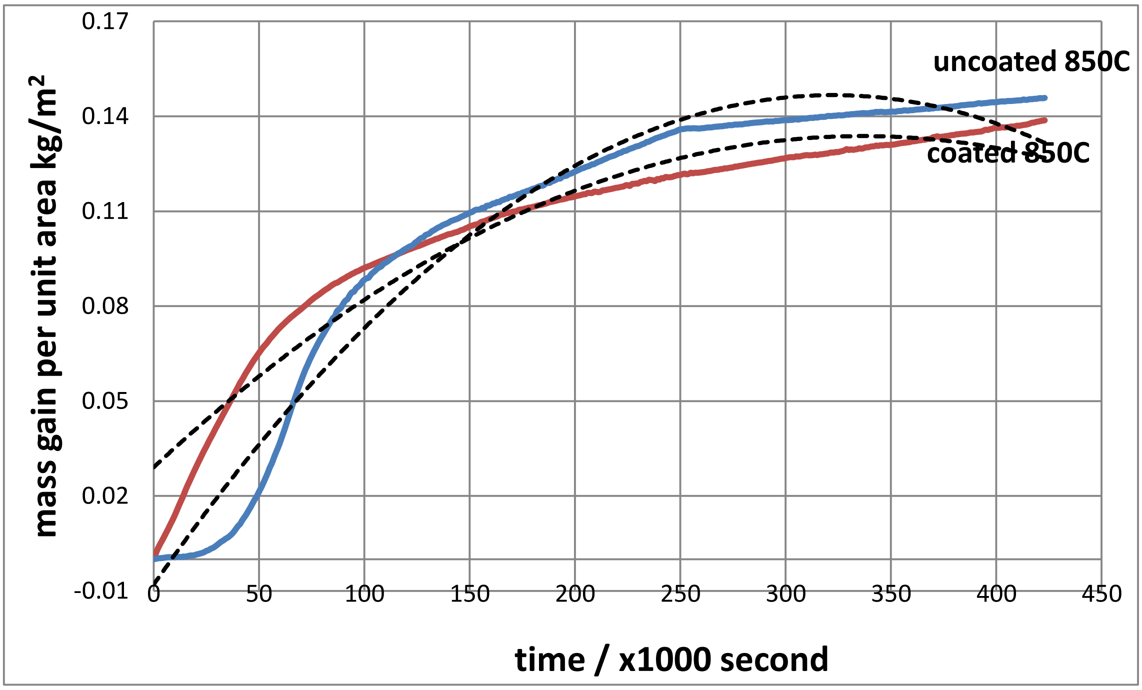

Figure 25, Isothermal oxidation kinetic plots and parabolic trend line of uncoated and coated SS 316L at 850 °C in combustion atmosphere.

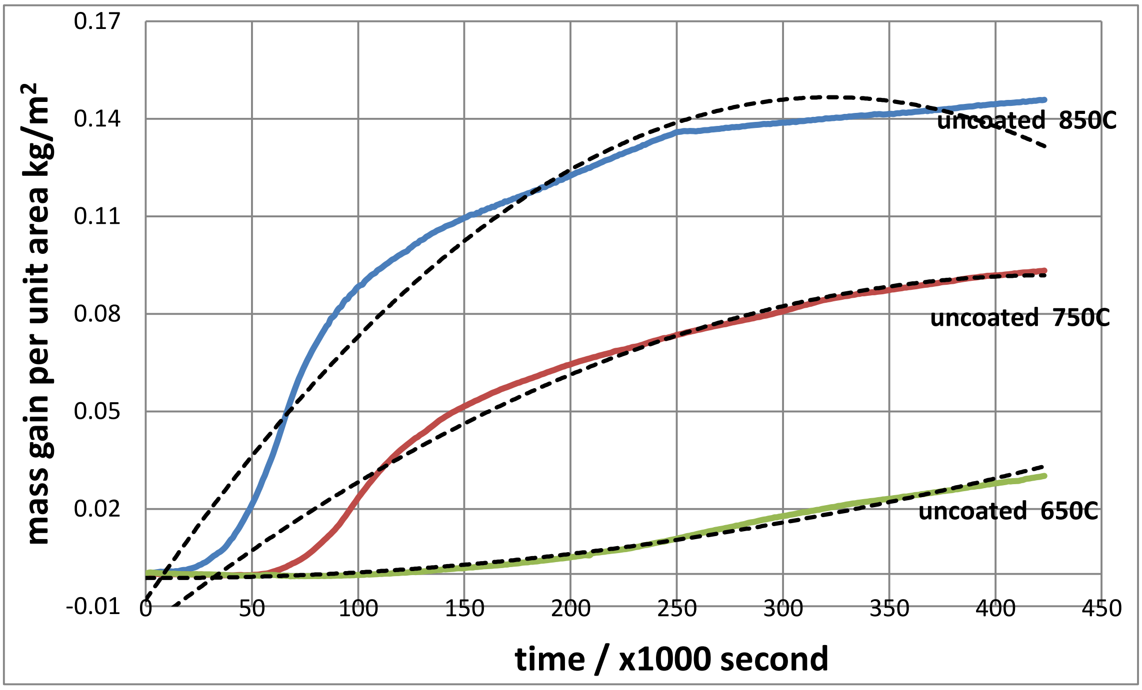

Figure 26, Isothermal oxidation kinetic plots and parabolic trend line of uncoated SS 316L at different temperature in combustion atmosphere.

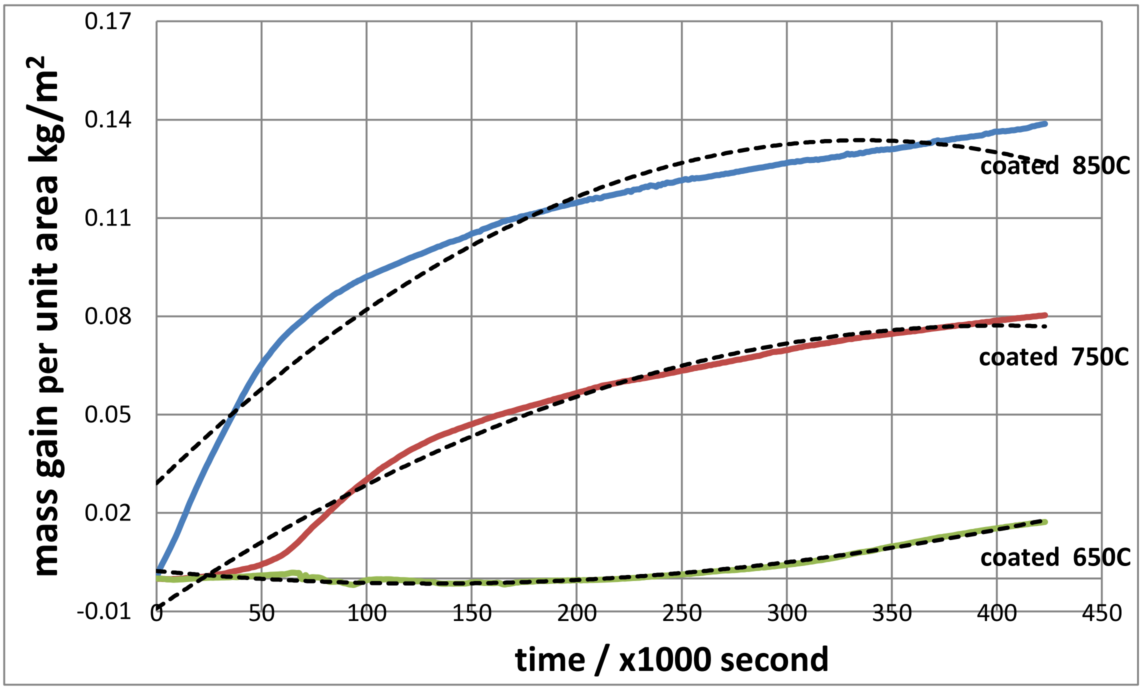

Figure 27, Isothermal oxidation kinetic plots and parabolic trend line of coated SS 316L at different temperature in combustion atmosphere.

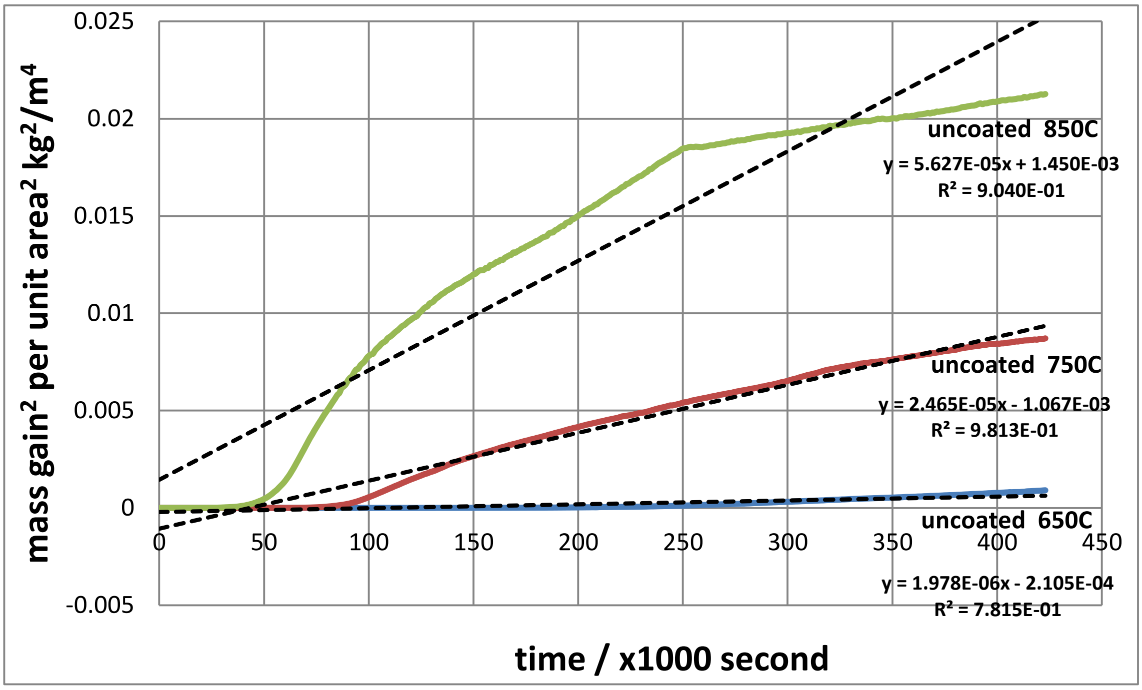

Figure 28, Oxidation rate constant K_p (first term coefficient of trend line)for the uncoated samples in combustion atmosphere.

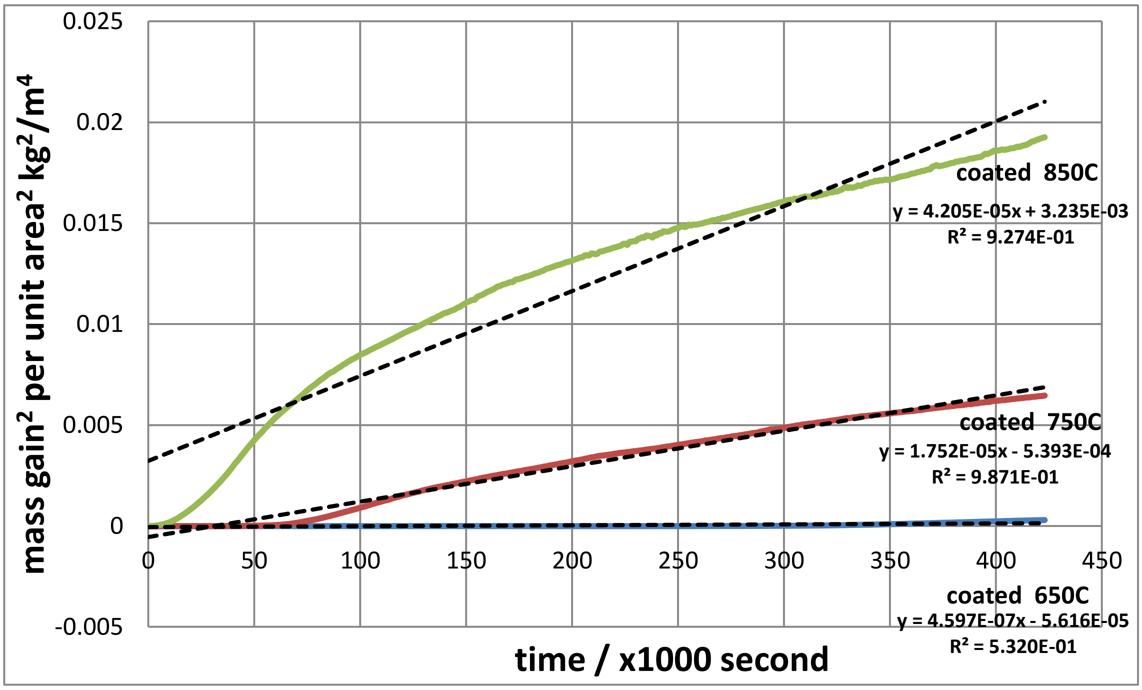

Figure 29, Oxidation rate constant K_p (first term coefficient of trend line)for the coated samples in combustion atmosphere.

Oxidation rate constant K_p $(kg^2/m^4)/s$	650 °C	750 °C	850 °C
uncoated	1.978×10^{-6}	2.456×10^{-5}	5.627×10^{-5}
coated	4.597×10^{-7}	1.752×10^{-5}	4.205×10^{-5}

Table 5, Matrix of oxidation rate constant K_p of combustion atmosphere oxidation.

According to mass change curves, it was clear that the coating in combustion atmosphere was not as effective as that in dry air. Coated and uncoated samples gained roughly the same mass at 850°C. As well as that at 850°C, the mass increase difference was not big enough to prove the effectiveness of the coating. At the lower temperature of 650°C, the situation seemed better, however the trend line showed that the oxidation rate was still high at the end of the test. Besides, the mass increasing curve was more complicated than that in the day air: the curve should be divided into 3 parts and each part should have its particular mechanism. The oxidation rate constant K_p and R^2 were given in the figure 28-29 and table 5. However the K_p did not match the curve very well and the reliability of K_p was doubtful. In a word, the oxidation in combustion atmosphere was not a simple procedure as that in dry air and was dominated by more complicated mechanisms. The possible mechanisms will be discussed later in this paper.

4.4 XRD characterization of High temperature oxidation

Eight of the 12 samples were characterized by XRD: coated and uncoated samples at 850 °C in dry air and all six samples in combustion atmosphere. Figure 30 and 31 show the XRD spectrum of uncoated and coated samples in combustion atmosphere respectively. Figure 32 shows the XRD spectrum in dry air at the temperature of 850 °C

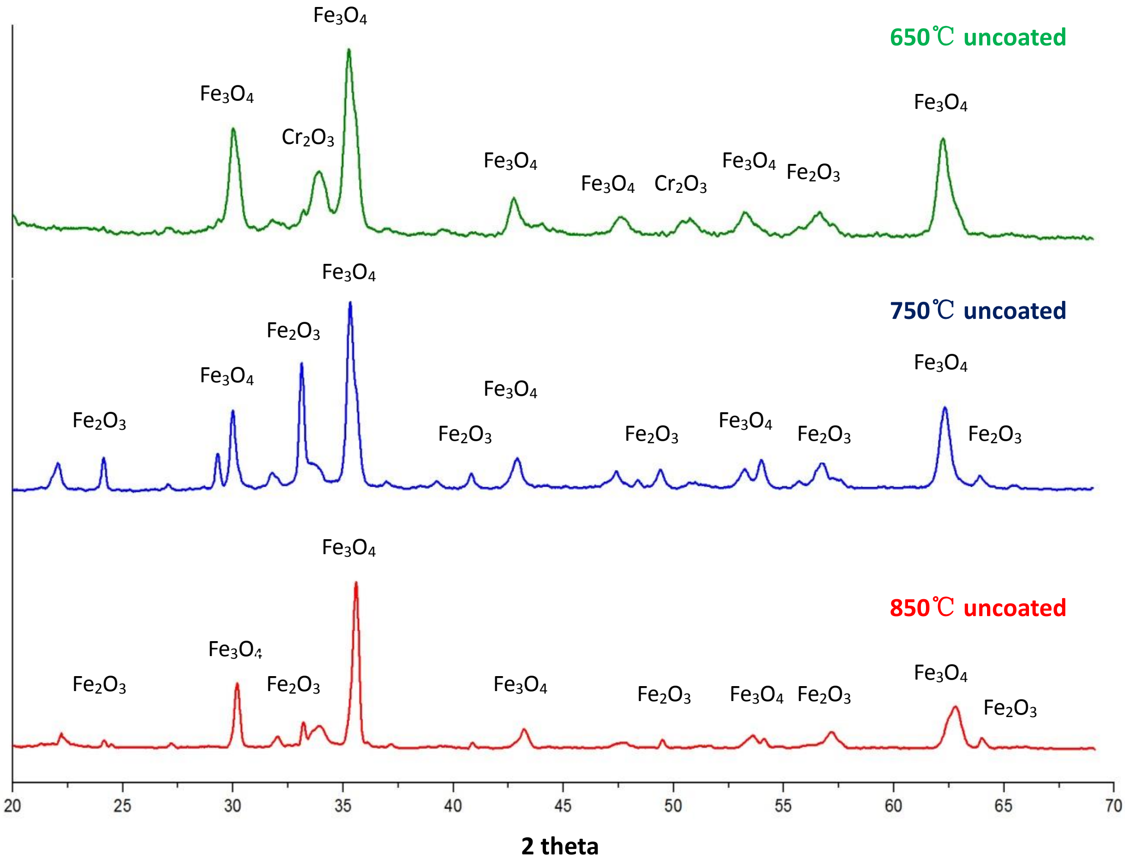

Figure 30, XRD spectrum of uncoated samples in combustion atmosphere. The oxidation temperature of sample a, b, c were 650°C, 750°C and 850°C respectively.

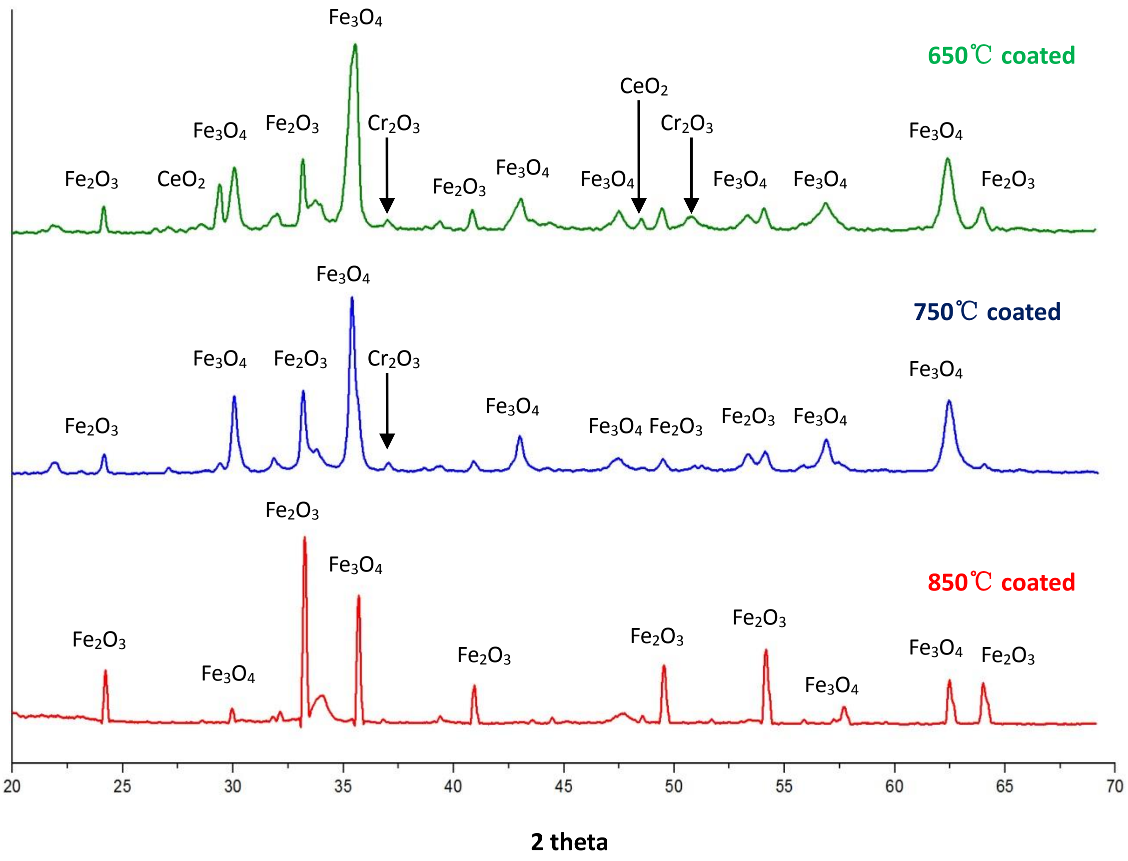

Figure 31, XRD spectrum of coated samples in combustion atmosphere. The oxidation temperature of sample a, b, c were 650°C, 750°C and 850°C respectively.

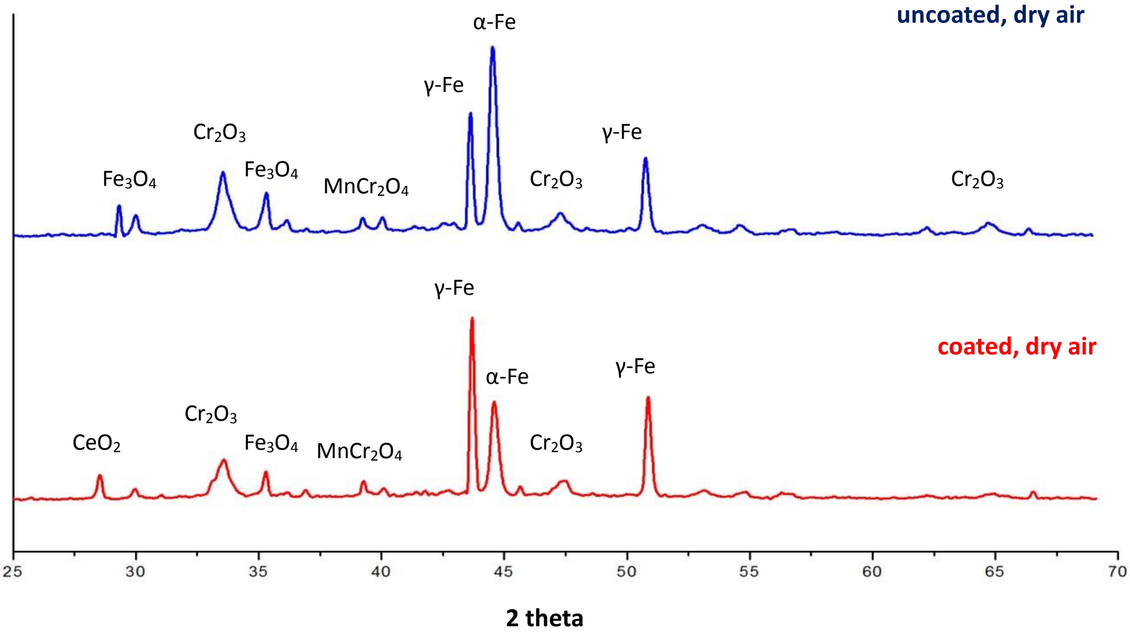

Figure 32, the XRD spectrum in dry air at the temperature of 850 °C

In dry air for both coated and uncoated samples, the matrix of samples was still austenitic Fe after oxidation. Cr in the stainless steel was concentrated and formed Cr_2O_3 as well as that Mn formed $MnCr_2O_4$ with Cr in the oxidation product. Small amount of Fe_3O_4 was detected as the result of iron oxidation. CeO_2 as coating material was also detected in the coated sample.

In the combustion atmosphere, all the Fe was oxidized to the Fe_2O_3 or Fe_3O_4 in the range of XRD detecting and no iron from the base metal was found. Besides, the surface of each sample was spalled during the oxidation in varying degree. Therefore, in some samples the Cr_2O_3 and $MnCr_2O_4$ were not detected and in others the peak of Cr_2O_3 was very weak. CeO_2 was only detected in 650°C due to the limited spalling of that samples.

4.5 Macro morphology of High temperature oxidation

Figure 33 and 34 show the macro photographs of dry air oxidation and combustion atmosphere oxidation samples. Some surface fragments are included if they were collected.

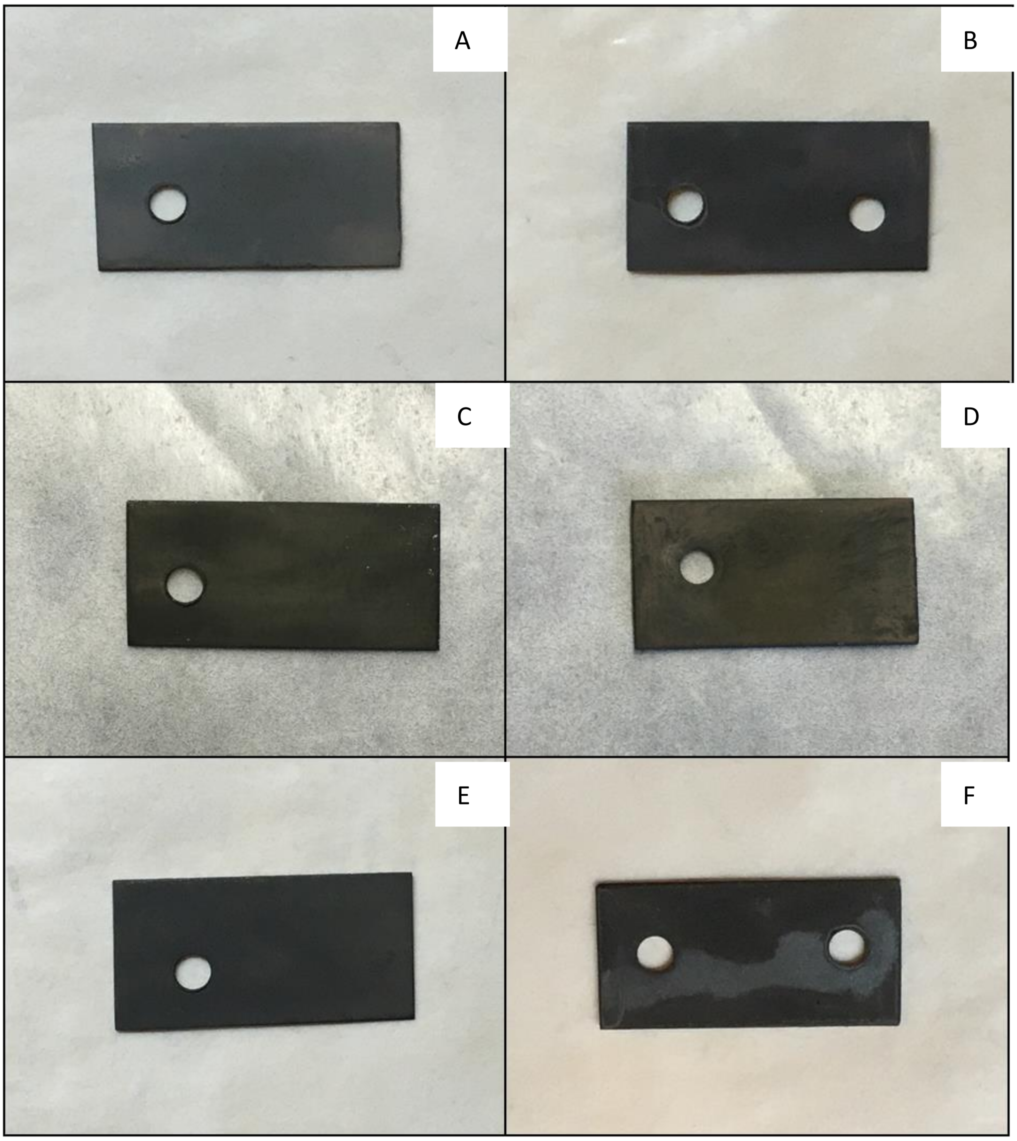

Figure 33, macro morphology of samples oxidized in the dry air. Sample A-F are 800°C uncoated, 800°C coated, 850°C uncoated, 850°C coated, 900°C uncoated and 900°C coated, respectively

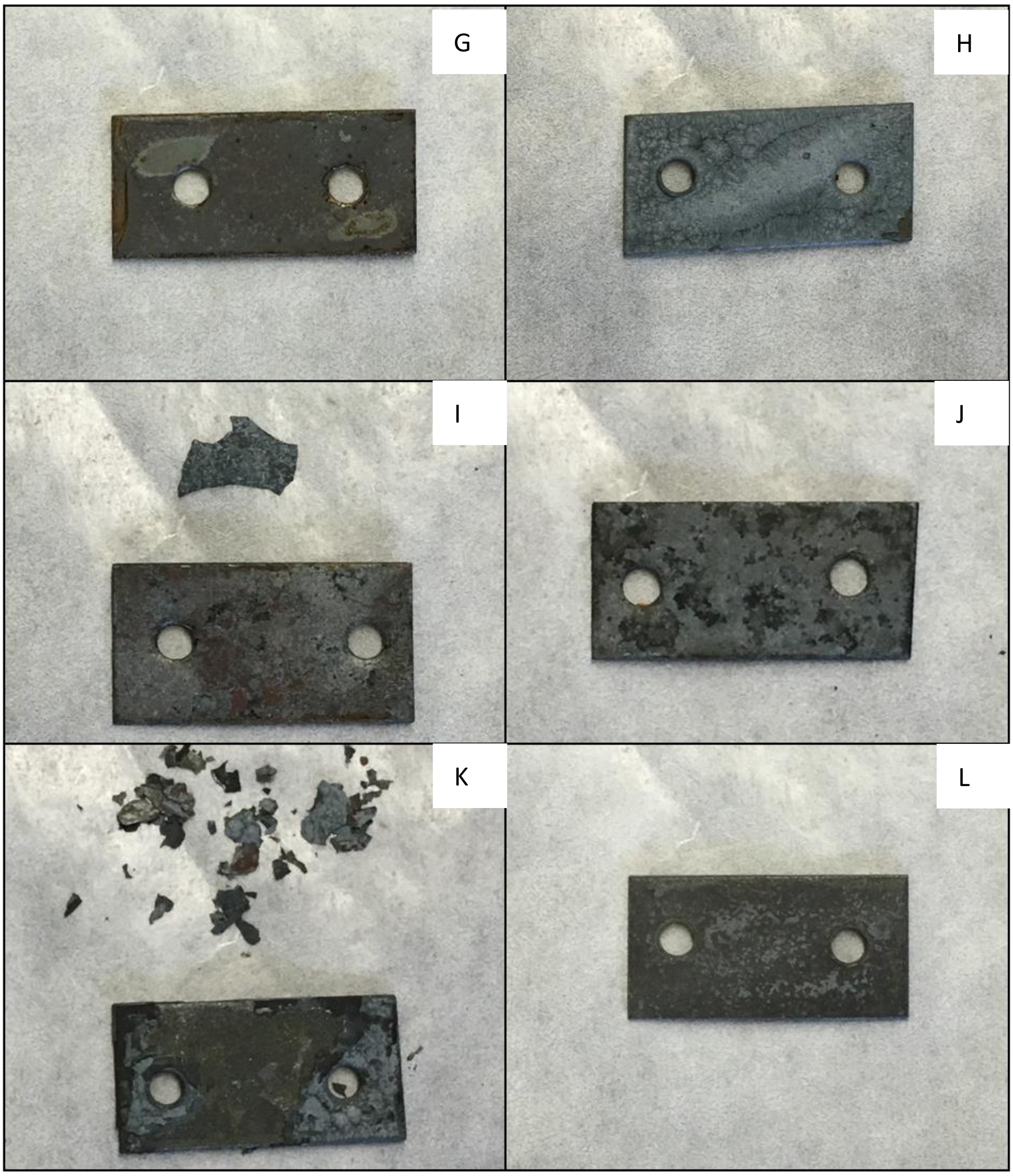

Figure 34, macro morphology of samples oxidized in combustion atmosphere. Sample G-L are 650°C uncoated, 650°C coated, 750°C uncoated, 750°C coated, 850°C uncoated and 850°C coated, respectively.

The samples oxidized in dry air did not have significant differences. The samples oxidized in combustion atmosphere had surface spalling to varying degrees. The surface of 650 °C was almost preserved with only minimal spalling, and the surface of 850°C had significant spalling.

4.6 SEM morphology of high temperature oxidation

The surface of dry air oxidized samples and the cross-section of dry air and combustion atmosphere oxidized samples were characterized by SEM. The surface of samples oxidized in combustion atmospheres were not characterized because of the rough and easily peeling off surface. Figure 35 shows surface micro morphology of coated sample oxidized at 850°C in dry air. Figure 36-37 show the cross-section micro morphology of coated and uncoated samples oxidized at 850°C in dry air, respectively. Figure 38-43 show the section micro morphology of 6 samples oxidized in combustion atmosphere.

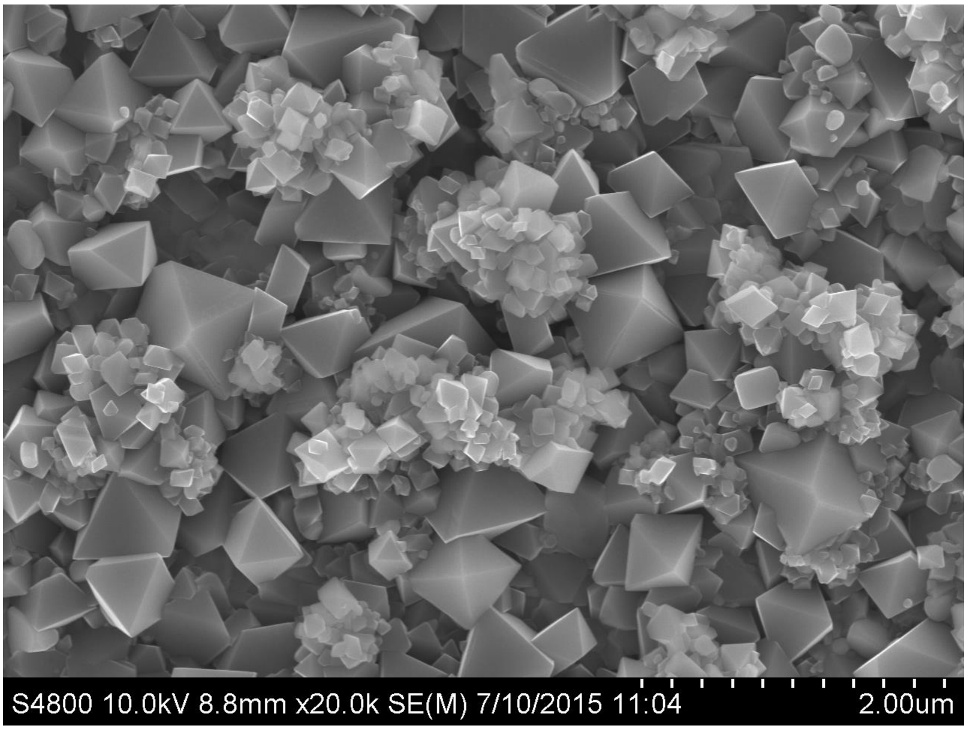

Figure 35, cross-section micro morphology of coated sample oxidized at 850°C

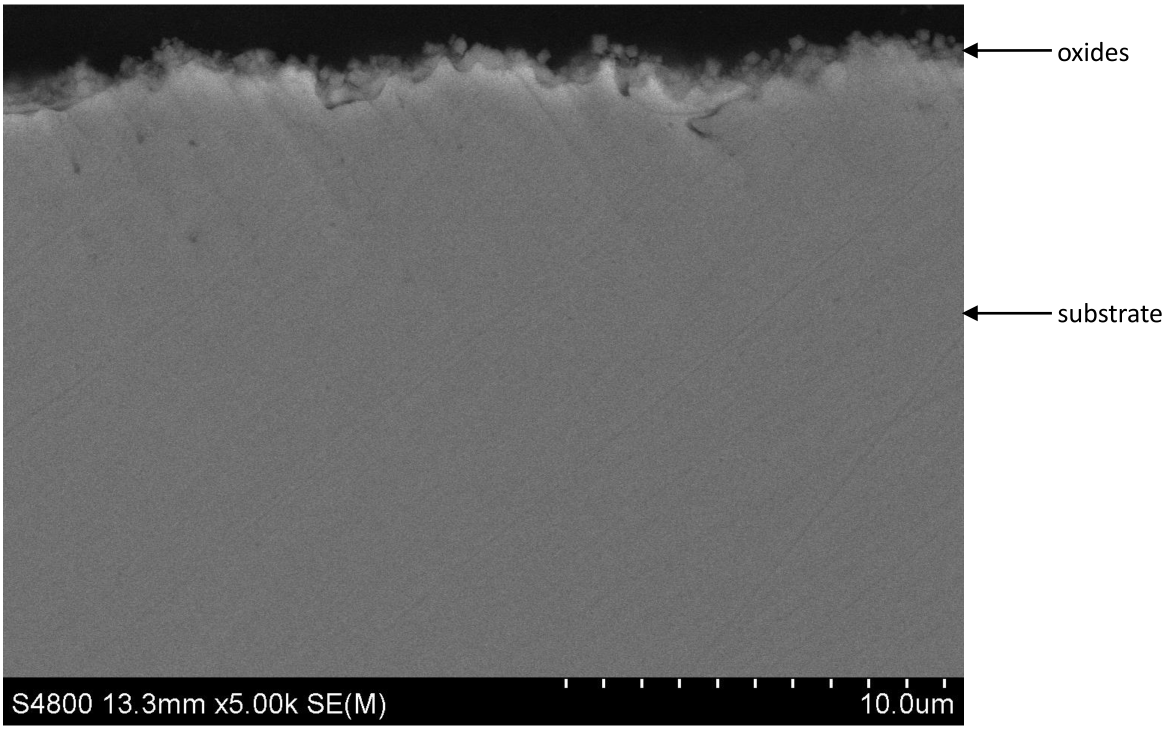

Figure 36, cross-section micro morphology of coated sample oxidized at 850°C in dry air.

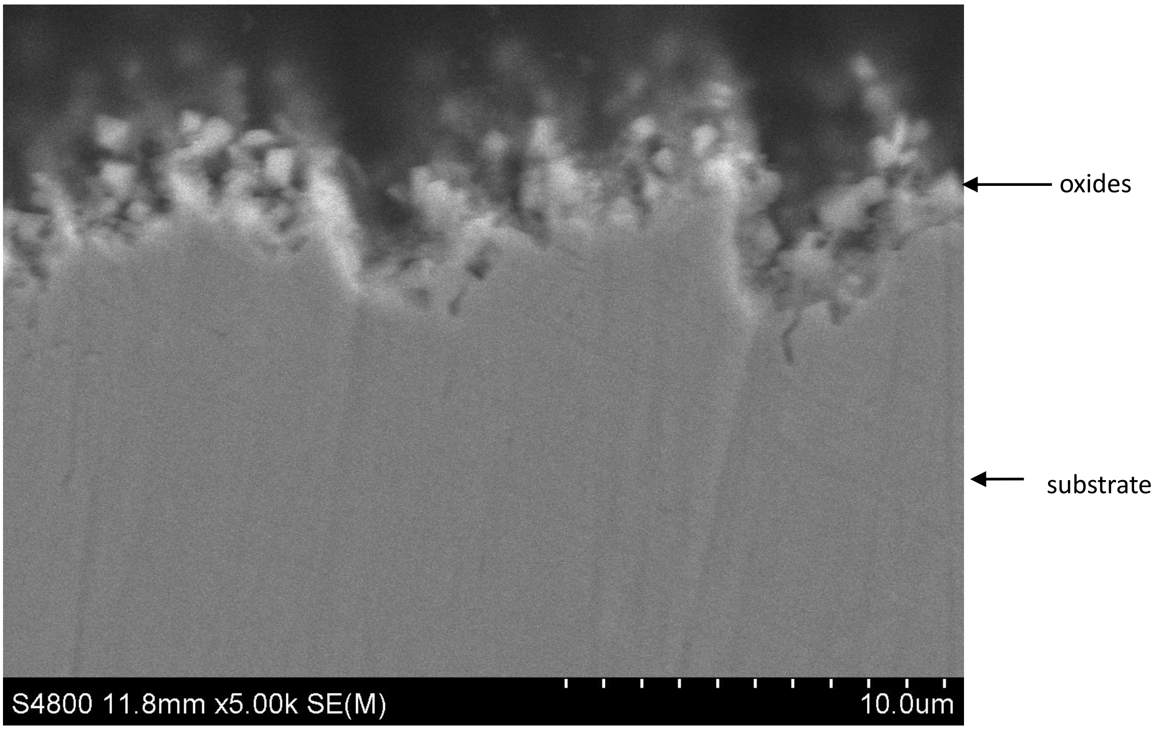

Figure 37, cross-section micro morphology of uncoated sample oxidized at 850°C in dry air

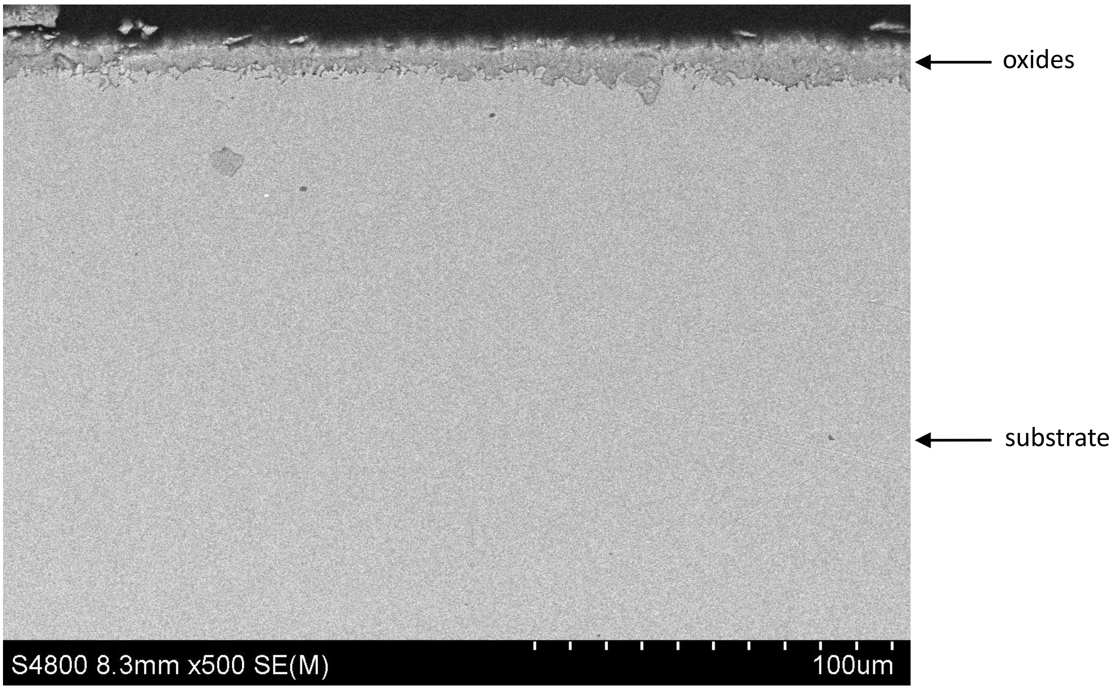

Figure 38, cross-section micro morphology of coated sample oxidized at 650°C in combustion atmosphere

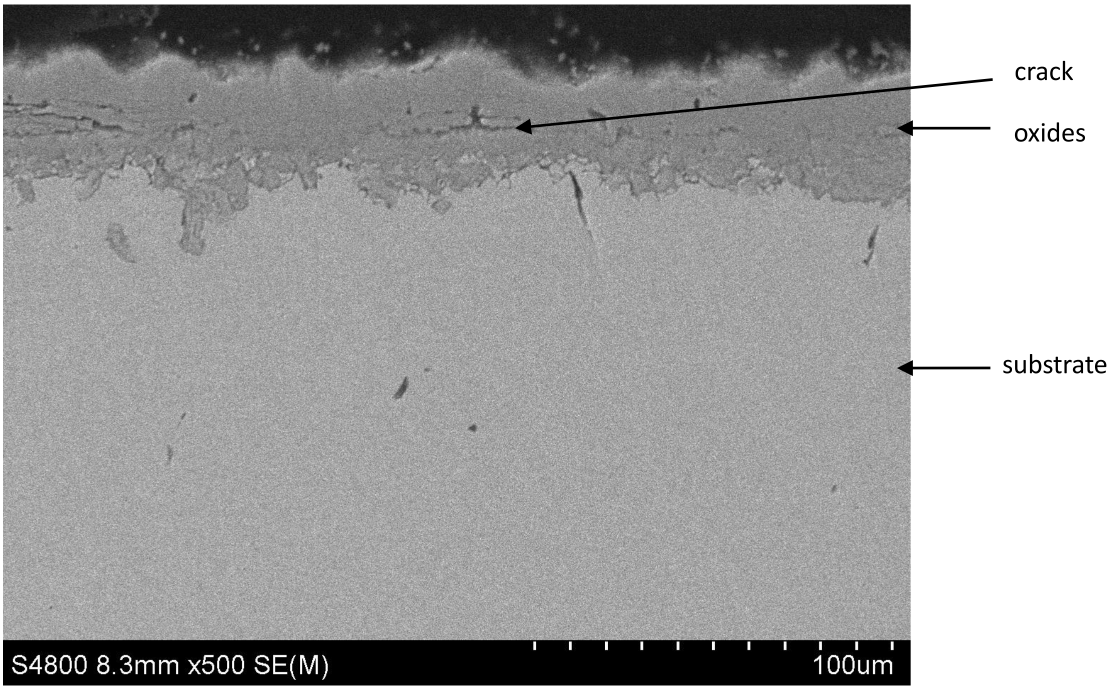

Figure 39, cross-section micro morphology of uncoated sample oxidized at 650°C in combustion atmosphere

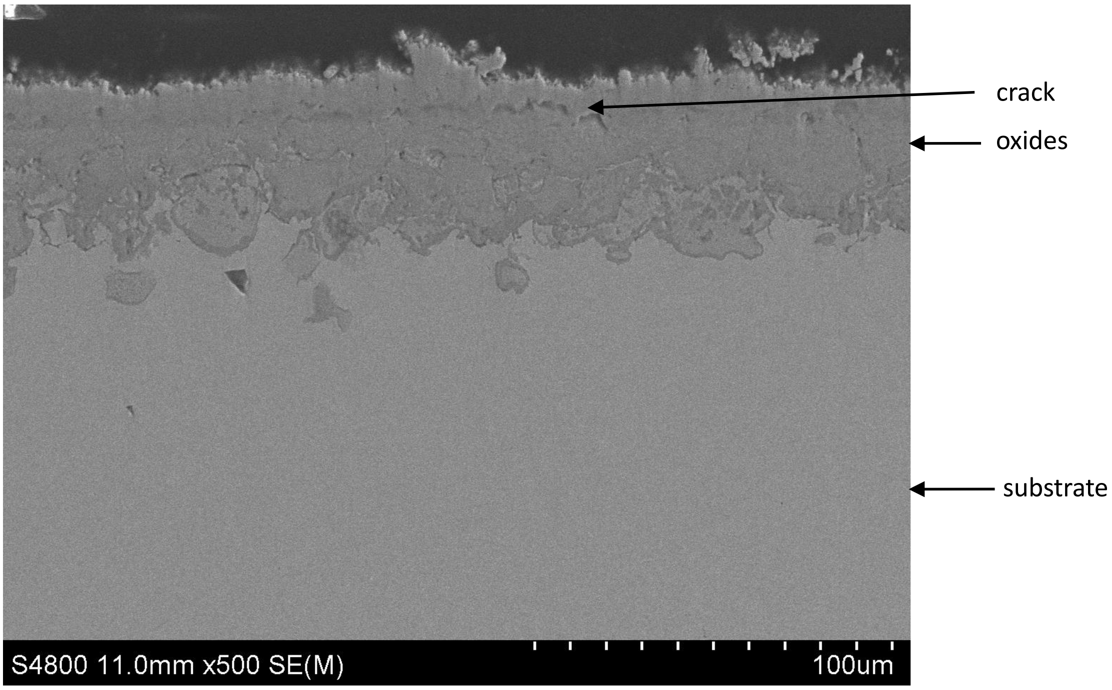

Figure 40, surface micro morphology of coated sample oxidized at 750°C in combustion atmosphere

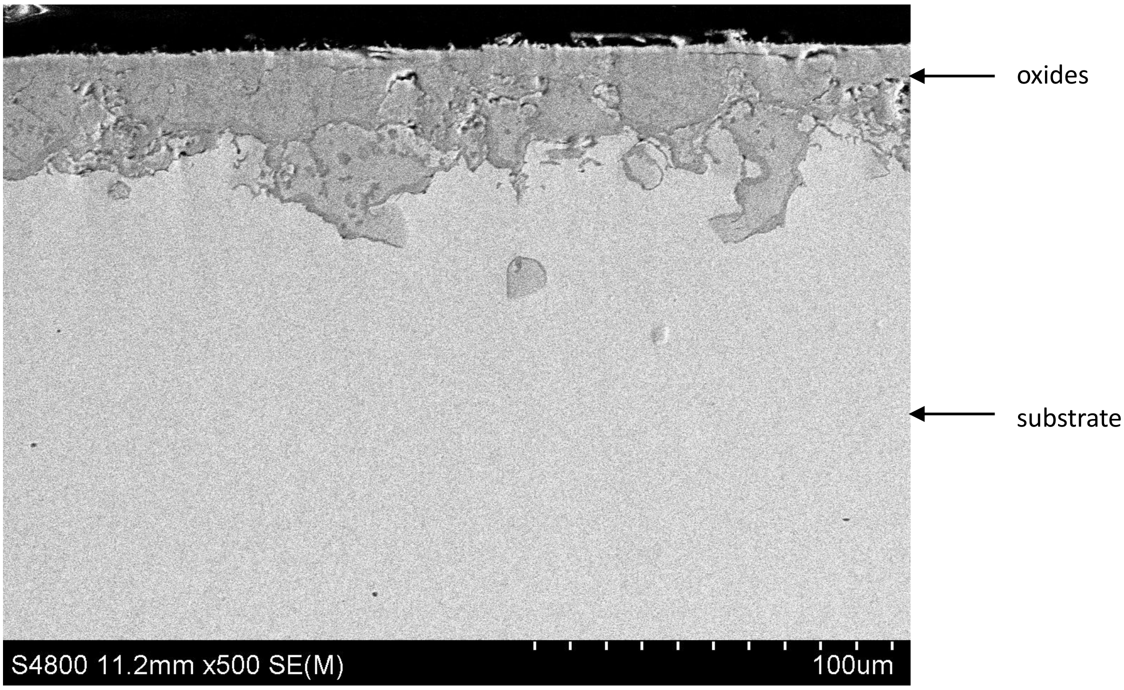

Figure 41, cross-section micro morphology of uncoated sample oxidized at 750°C in combustion atmosphere

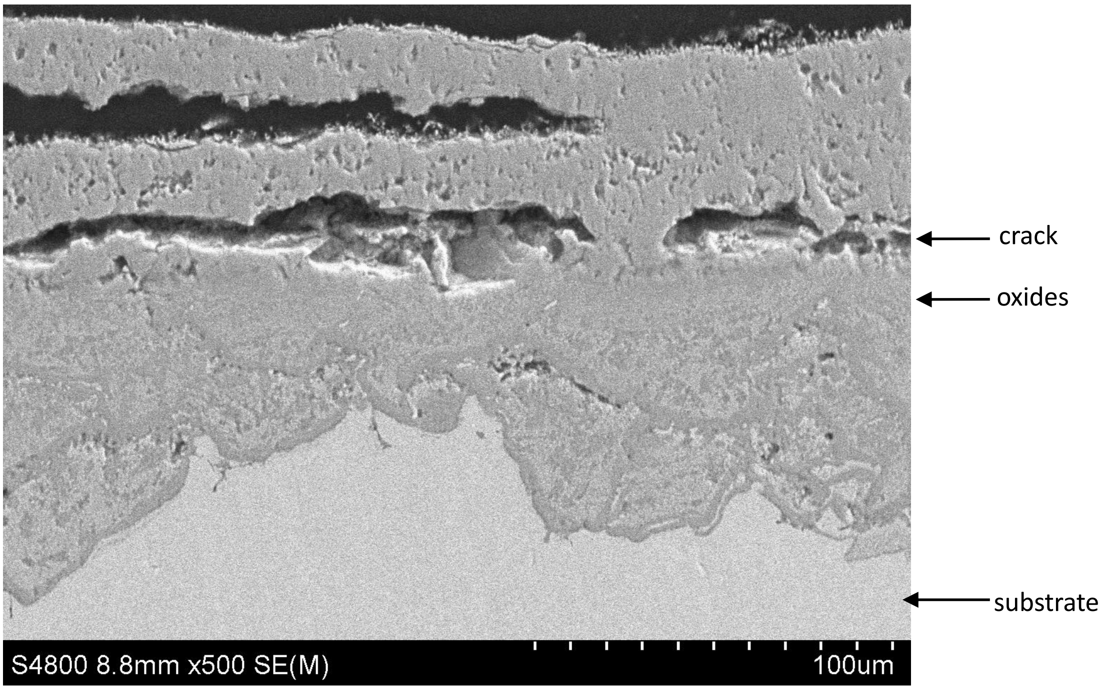

Figure 42, cross-section micro morphology of coated sample oxidized at 850°C in combustion atmosphere

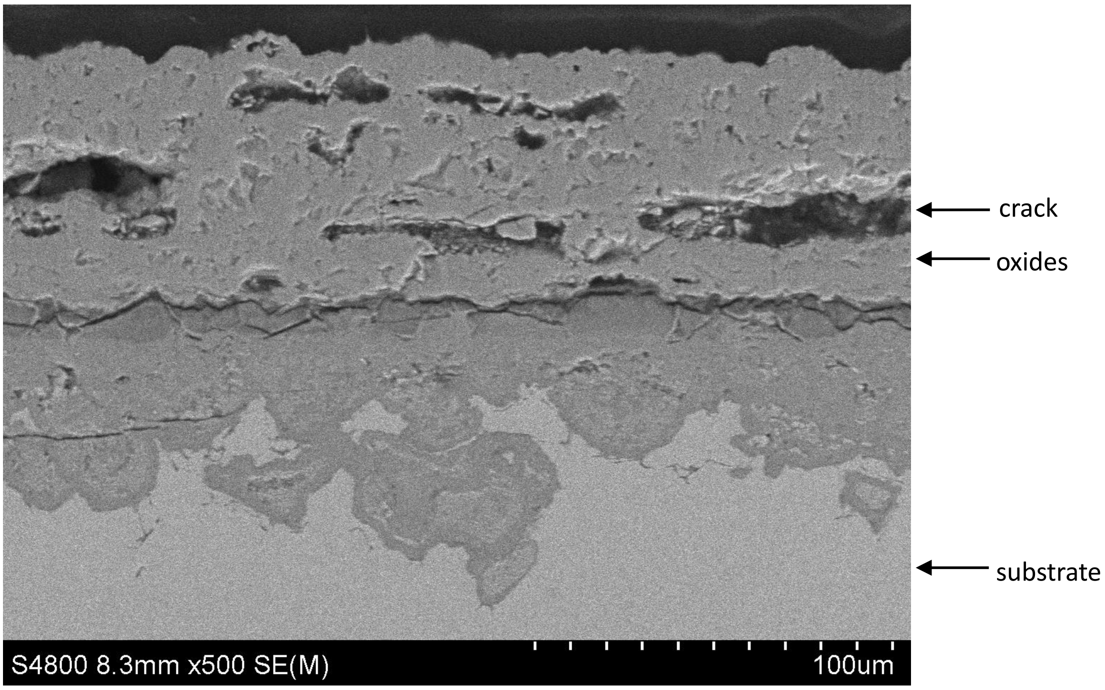

Figure 43, cross-section micro morphology of uncoated sample oxidized at 850°C in combustion atmosphere

5 Discussions

Generally speaking, it is not difficult to synthesize 10nm level nano ceria particles by the microemulsion method. The difficulties are how to prevent the agglomeration of nanoparticles and how to remove the surfactant without hurting the separation of nanoparticles. Because of the inherent instability of nanoparticles, agglomeration can occur at any stage: synthesis, preservation, coating or drying. In this research, all these stages were considered and a possible method to overcome all of these difficulties was eventually founded.

Keeping the solution cold could reduce the molecular thermal motion and that provided a part of contribution to anti-agglomeration. Stirring speed was the critical factor on controlling the particle size and agglomeration during the synthesis. A lower stirring speed could cause serious agglomeration and a higher stirring speed could completely prevent the agglomeration. However, excess high stirring speed was not the optimal situation. The excess high stirring speed could also stop $Ce(OH)_4$ transforming to CeO_2 as well as make it impossible to remove the surfactant (AOT) from the solution. A moderate stirring speed was required, and in this research it was about 500 revolutions per minute. Essentially it was a balance between agglomeration degree and precipitation speed. Another balance in the research was between purity of CeO_2 and the agglomeration degree: with more AOT was extracted, more serious the agglomeration occurred. In the research, the time was limited and the optimal solution was not found. Anyway, an acceptable procedure was obtained, the particle size was about 2-3 nm and the agglomeration size was under 30 nm which was proved by XRD spectrum in figure 9 and TEM micrograph in figure 10. Besides, this method made long time preservation possible, the particles were stable in the solution for more than 6 months.

Improved coating method also helped the separation of nanoparticles. With using a slide motor, slow and uniform motion made very little liquid left on the substrate at one time. That helped preventing agglomeration during the drying. Slide motor made the coating thickness controllable by setting the cycle numbers and speed. In this research, a thin coating layer was applied with the cycle numbers was 5 and motor speed at 0.05mm/sec.

The oxidation in dry air could be predicated; parabolic law and coating was successful in improving the oxidation resistance. A Cr_2O_3 film was formed on coated and uncoated samples to prevent the further oxidation which was shown by figure 35-37.

On the other hand, the oxidation in combustion atmosphere was much more complicated. According to vapor water- mediated volatilization theory[12], Cr_2O_3 was volatilized into $CrO_2(OH)_2$ gas in water vapor. This volatilization could destroy the protective Cr_2O_3 film and substantially altered the oxidation kinetics. The result showing in the figure was the dramatic mass increasing and thick oxides layer.

The mass gaining curve in figure 23-25 shows the whole oxidation process should be divided into 3 parts. The first part was initial low oxidation rate, it lasted about 30 hours for 650°C, 15 hours for 750°C and about 8 hours for 850°C. The oxidation rate of this part was just little higher (about 30% from the 850°C data) than that in dry air. The second part was a dramatic increasing of oxidation rate and lasted about another 40 hours for each samples. The third part was a constant oxidation rate until the end of the test. Here a possible assumption is proposed: Volatilization of Cr_2O_3 proceeds slowly and it takes hours to volatilize the whole Cr_2O_3 film. Before all the Cr_2O_3 is consumed, the rest Cr_2O_3 film can still protect the substrate effectively. After volatilization, the iron rich substrate is exposed and result in sharp oxidation.

In the research, CeO_2 coating was applied on the surface to test whether it could help the protecting. The result showed that the coating retarded the protecting at 850°C because the slow oxidation stage disappeared. At 750°C, the nano-ceria coating has very limited influence on the oxidation. At 650°C, the nano-ceria coating extended the slow oxidation stage from 30 hours to 60 hours. It seemed that there was a strong temperature relevance and the coating performed better at lower temperature.

Up to now, we are still not clear about the mechanism of CeO_2 on Cr_2O_3 when water vapor is involved. In some conditions it helps and in some conditions it retards. The meaning of this research is we find that in combustion atmosphere, the oxidation of stainless steel has a initial stage with low oxidation rate. Coating of materials can have some effects on that initial stage. So it can be a possible method to protect the Cr_2O_3 from volatilization by coating something and just let the stabilized Cr_2O_3 to protect the substrate in combustion atmosphere.

6 Conclusions

Conclusions based on the experimental result include:

- Non-agglomerated Ceria nanoparticles were synthesize by a microemulsion method with the average particle size of 2-3nm.
- Stirring speed during synthesis has a critical influence of the particle size and agglomeration degree. Higher stirring speed leads to smaller particle size and fewer agglomeration.
- The AOT surfactant can be removed by a precipitation method.
- Dip coating by using slide motor creates a uniform and non-agglomerated coating film.
- Ceria coating can improve the SS 316L oxidation performance in dry air at the temperature from 800° C to 900°C.
- The oxidation mechanism in combustion air is different from that in dry air. Volatilization of Cr_2O_3 cause serious oxidation.
- Volatilization of Cr_2O_3 can last for hours and ceria coating has some effect on that stage. Coating works better at lower temperature.
- It can be a possible method to protect Cr_2O_3 from volatilization by coating something.

7 References

[1] R. J. Hussey, P. Papaiacovou, J. Shen, D. F. Mitchell, M. J. Graham, Materials Science and Engineering: A 1989, 120, 147.

[2] H. F. Lopez, H. Mendoza-Del Angel, Materials Chemistry and Physics 2014, 146, 204.

[3] T. N. Rhys-Jones, H. J. Grabke, H. Kudielka, Corrosion Science 1987, 27, 49.

[4] S. Patil, S. C. Kuiry, S. Seal, R. Vanfleet, Journal of Nanoparticle Research, 4, 433.

[5] R. Thanneeru, S. Patil, S. Deshpande, S. Seal, Acta Materialia 2007, 55, 3457.

[6] E. P. Murray, T. Tsai, S. A. Barnett, Nature 1999, 400, 649.

[7] B. Rotavera, A. Kumar, S. Seal, E. L. Petersen, Proceedings of the Combustion Institute 2009, 32, 811.

[8] J. Antill, K. Peakball, J. Iron Steel Inst. (London), 205: 1136-42 (Nov. 1967).

[9] J. Stringer, Materials Science and Engineering: A 1989, 120, 129.

[10] L. Tye, N. A. El-Masry, T. Chikyow, P. McLarty, S. M. Bedair, Applied Physics Letters 1994, 65, 3081.

[11] P. Kofstad, *High-temperature oxidation of metals*, Wiley, 1966. P112.

[12] P. J. Meschter, E. J. Opila, N. S. Jacobson, Annual Review of Materials Research 2013, 43, 559.

[13] M. P. Brady, M. Fayek, J. R. Keiser, H. M. Meyer Iii, K. L. More, L. M. Anovitz, D. J. Wesolowski, D. R. Cole, Corrosion Science 2011, 53, 1633.

[14] H. Asteman, J. E. Svensson, M. Norell, L. G. Johansson, Oxidation of Metals, 54, 11.

[15] N. Mu, K. Jung, N. M. Yanar, F. S. Pettit, G. R. Holcomb, B. H. Howard, G. H. Meier, Oxidation of Metals 2013, 79, 461.

[16] M. Sun, X. Wu, Z. Zhang, E.-H. Han, Corrosion Science 2009, 51, 1069.

[17] N. Birks, G. H. Meier, F. S. Pettit, *Introduction to the high temperature oxidation of metals*, Cambridge University Press, 2006.

[18] C. Wagner, Z. Phys. Chem., 21(1933), 25.

[19] C. Wagner, J. Electrochem Soc. 99, 1952 p.369

[20] P. Kofstad, High Temperature Corrosion, Elsevier, London, 1988, p. 1-558.

[21] X. Zheng, D. Young, Oxidation of Metals 1994, 42, 163.

[22] J. Mougin, T. Le Bihan, G. Lucazeau, Journal of Physics and Chemistry of Solids 2001, 62, 553.

[23] D. Lussana, D. Baldissin, M. Massazza, M. Baricco, Oxidation of Metals 2013, 81, 515.

[24] C. Wagner, Atom Movements, 1953, p. 153

[25] C. R. Hammond (2000). The Elements in Handbook of Chemistry and Physics 81st edition, CRC press.

[26] Patnaik, Pradyot (2003). Handbook of Inorganic Chemical Compounds. McGraw-Hill. p. 199-200.

[27] A. Trovarelli, Catalysis Reviews 1996, 38, 439.

[28] P. Papaiacovou, R. Hussey, D. Mitchell, M. Graham, Corrosion Science 1990, 30, 451.

[29]. Artur Goldschmidt and Hans-Joachim Streitberger, *BASF Handbook on Basics of Coating Technology*, William Andrew Inc., 2003

[30] A. A. Tracton, *Coatings technology handbook*, CRC press, 2005.

[31] National Research Council Staff. Coatings for High-Temperature Structural Materials : Trends and Opportunities. Washington, US: National Academies Press, 1998. ProQuest ebrary. Web. 25 April 2016.